The Astrophysical Journal Letters, 1000:L18 (16pp), 2026 March 20 https://doi.org/10.3847/2041-8213/ae4c88

The X-Ray Dot: Exotic Dust or a Late-stage Little Red Dot?

Raphael E. Hviding[1], Anna de Graaff[1,2,14], Hanpu Liu (刘翰溥)[3], Andy D. Goulding[3], Yilun Ma (马逸伦)[3], Jenny E. Greene[3], Leindert A. Boogaard[4], Andrew J. Bunker[5], Nikko J. Cleri[6,7,8], Marijn Franx[4], Michaela Hirschmann[9], Joel Leja[6,7,8], Jorryt Matthee[10], Rohan P. Naidu[11,15], David J. Setton[3,16], Hannah Übler[12], Giacomo Venturi[13], and Bingjie Wang (王冰 洁)[3,17]

[1] Max-Planck-Institut für Astronomie, Königstuhl 17, D-69117 Heidelberg, Germany; hviding@mpia.de
[2] Center for Astrophysics, Harvard & Smithsonian, 60 Garden Street, Cambridge, MA 02138, USA
[3] Department of Astrophysical Sciences, Princeton University, Princeton, NJ 08544, USA
[4] Leiden Observatory, Leiden University, PO Box 9513, NL-2300 RA Leiden, The Netherlands
[5] Department of Physics, University of Oxford, Denys Wilkinson Building, Keble Road, Oxford OX1 3RH, UK
[6] Department of Astronomy & Astrophysics, The Pennsylvania State University, University Park, PA 16802, USA
[7] Institute for Computational & Data Sciences, The Pennsylvania State University, University Park, PA 16802, USA
[8] Institute for Gravitation and the Cosmos, The Pennsylvania State University, University Park, PA 16802, USA
[9] Institute for Physics, Laboratory for Galaxy Evolution and Spectral modelling, Ecole Polytechnique Federale de Lausanne, Observatoire de Sauverny, Chemin Pegasi 51, 1290 Versoix, Switzerland
[10] Institute of Science and Technology Austria (ISTA), Am Campus 1, 3400 Klosterneuburg, Austria
[11] MIT Kavli Institute for Astrophysics and Space Research, 70 Vassar Street, Cambridge, MA 02139, USA
[12] Max-Planck-Institut für extraterrestrische Physik, Gießenbachstraße, Germany
[13] Scuola Normale Superiore, Piazza dei Cavalieri 7, I-56126 Pisa, Italy

Received 2026 January 14; revised 2026 February 19; accepted 2026 March 1; published 2026 March 16

Abstract

JWST's "little red dots" (LRDs) are increasingly interpreted as active galactic nuclei (AGN) obscured by dense thermalized gas rather than dust as evidenced by their X-ray weakness, blackbody-like continua, and Balmer line profiles. Key questions are how LRDs connect to standard UV-luminous AGN, whether transitional phases exist, and whether they are observable. We present the "X-ray dot" (XRD), a compact source at $z = 3.28$ observed by the NIRSpec Wide Guaranteed Time Observation survey. The XRD exhibits LRD hallmarks: a blackbody-like ($T_{\rm eff} \simeq 6400\,{\rm K}$) red continuum, a faint but blue rest-UV excess, falling mid-IR emission, and broad Balmer lines (FWHM ~ 2700–$3200\,{\rm km\,s^{-1}}$). Unlike LRDs, however, it is remarkably X-ray luminous ($L_{2-10\,{\rm keV}} = 10^{44.18}\,{\rm erg\,s^{-1}}$) and has a continuum inflection that is blueward of the Balmer limit. We find that the red rest-optical and blue mid-IR continuum cannot be reproduced by standard dust-attenuated AGN models without invoking extremely steep extinction curves, nor can the weak mid-IR emission be reconciled with well-established X-ray–torus scaling relations. We therefore consider an alternative scenario: the XRD may be an LRD in transition, where the gas envelope dominates the optical continuum but optically thin sight lines allow X-rays to escape. The XRD may thus provide a physical link between LRDs and standard AGN, offering direct evidence that LRDs are powered by supermassive black holes and providing insight into their accretion properties.

Unified Astronomy Thesaurus concepts: Active galactic nuclei (16); X-ray quasars (1821); High-redshift galaxies (734)

1. Introduction

JWST's "little red dots" (LRDs; J. Matthee et al. 2024) are a ubiquitous population of high-redshift ($z \gtrsim 4$) compact sources with unique spectrophotometric properties (e.g., V. Kokorev et al. 2024; D. D. Kocevski et al. 2025; R. E. Hviding et al. 2025). Characterized by V-shaped rest-UV–optical spectral energy distributions (SEDs) and broad Balmer emission lines, these objects were, at least in part, initially interpreted as dust-reddened active galactic nuclei (AGN; e.g., J. Matthee et al. 2024). However, LRDs are notably X-ray undetected, remaining faint even in stacks (e.g., M. Yue et al. 2024; T. T. Ananna et al. 2024), and lack the strong mid-infrared detections expected from a hot dust torus (e.g., C. C. Williams et al. 2024; C. M. Casey et al. 2024; H. B. Akins et al. 2025; D. J. Setton et al. 2025). Furthermore, many LRDs exhibit strong spectral breaks near the Balmer limit, extreme Balmer decrements (>10), and high rates of Balmer line absorbers (>30%; I. Juodžbalis et al. 2024; J. Matthee et al. 2024; D. J. Setton et al. 2025; B. Wang et al. 2024; F. D'Eugenio et al. 2025; A. de Graaff et al. 2025b; A. Torralba et al. 2026) that are difficult to reconcile with dust attenuation models.

A new paradigm proposes that LRDs are AGN embedded in dense, optically thick gas rather than dust. In this "black hole star" scenario, the red continuum originates from an optically thick gas envelope with similarities to a stellar atmosphere, yielding a Balmer break via absorption from collisionally excited hydrogen populating the $n = 2$ level (A. de Graaff et al. 2025c; K. Inayoshi & R. Maiolino 2025; X. Ji et al. 2025; R. P. Naidu et al. 2025). Moreover, additional dense gas signatures are seen in Balmer line profiles, including line-of-sight absorbers (e.g., I. Juodžbalis et al. 2024; F. D'Eugenio et al. 2025) and extended

---

[14] Clay Fellow.
[15] MIT Pappalardo Fellow.
[16] Brinson Prize Fellow.
[17] NHFP Hubble Fellow.

wings that are sometimes consistent with electron-scattering broadening (e.g., S.-J. Chang et al. 2026; V. Rusakov et al. 2026). These features need not arise from a single component, but instead can reflect a multiphase medium with distinct emitting, absorbing, and scattering regions. Such gas-rich environments can naturally suppress X-ray emission via high column densities, although super-Eddington accretion has also been proposed to explain the X-ray weakness of LRDs through intrinsically steeper X-ray spectra (e.g., A. Tortosa et al. 2023; E. Lambrides et al. 2024; P. Madau & F. Haardt 2024).

If LRDs indeed represent a phase of rapid, gas-enshrouded accretion, they may play a central role in the mass assembly of supermassive black holes (SMBHs) and potentially reconcile the discovery of massive SMBHs in the early Universe ($z \gtrsim 5$; e.g., K. Inayoshi 2025). However, a key open question remains: how are LRDs linked to the well-studied population of X-ray and UV-luminous accreting SMBHs at later cosmic times? While stacking analyses indicate that a large fraction of LRDs are X-ray weak, it remains unclear whether this applies to the entire population, particularly given their relative faintness. Alternatively, the sharp decline in the number density of LRDs around $z \sim 3$ (V. Kokorev et al. 2024; D. D. Kocevski et al. 2025; Y. Ma et al. 2025b) may suggest a transition in accretion mode or obscuration, raising the question of whether an intermediate evolutionary phase should be observable as LRDs evolve into the UV-luminous quasar population.

In the black hole star scenario, the envelope should eventually disperse as the SMBH accretion rate exceeds that of the gas infall (D. Kido et al. 2025). One may therefore expect a transitionary phase where the X-rays can escape as sight lines to the accreting black hole begin to clear. Recently, S. Fu et al. (2025) identified two LRD candidates at $z \sim 2.9$, dubbed the "Forges," that exhibit broad rest near-IR emission lines and a photometric V shape alongside intense X-ray, radio, and mid-IR emission, which they suggest mark a transitionary LRD phase with elements of both UV-luminous quasars and LRDs. We note that Forge II was independently reported in Z.-J. Li et al. (2025) as `cid_414`. However, unlike any LRD observed to date, these sources reported by S. Fu et al. (2025) and Z.-J. Li et al. (2025) show strong evidence for hot dust emission. Moreover, their bolometric luminosities ($\sim 10^{46}$ erg s^{-1}) are >1 dex higher than typical LRDs ($\sim 10^{43}$–10^{45} erg s^{-1}), raising the question of where precisely these objects fit into LRD evolution.

In this Letter, we present 3DHST-AEGIS-12014, hereafter the "X-ray dot" (XRD), a compact source at $z = 3.28$ with a blackbody-like red rest-optical continuum ($L_{\rm bol} \sim 5 \times 10^{44}$ erg s^{-1}), broad Balmer emission lines, and a falling mid-IR continuum, all features typically associated with LRDs. Notably, the XRD exhibits luminous, and potentially variable, X-ray emission. In Section 2, we present the existing CFHT/Hubble Space Telescope (HST)/Spitzer photometric data, NIRSpec/PRISM spectroscopy obtained as a part of the Wide Guaranteed Time Observation (GTO) survey (M. V. Maseda et al. 2024), and Chandra X-ray observations used in this work. We first consider the scenario that this source is a dust-reddened AGN in Section 3, but we show that standard dust prescriptions fail to explain the XRD's properties. We therefore explore the possibility that the XRD is a late-stage LRD and discuss the implied physical conditions of the gas in Section 4. Finally, we present our summary and discussion in Section 5. We assume a flat ΛCDM cosmology with $\Omega_m = 0.3$ and $H_0 = 70$ km s^{-1} Mpc^{-1}.

2. The X-Ray Dot

2.1. Photometry

The All-Wavelength Extended Groth Strip International Survey (AEGIS; M. Davis et al. 2007) provides a wealth of photometry from the X-ray through submillimeter across the Extended Groth Strip (EGS). We obtain optical through mid-IR photometry of the XRD spanning 0.6–24 μm (CFHT WIRCam, HST ACS and WFC3, and Spitzer IRAC and MIPS) from the public 3D-HST photometric catalogs (G. B. Brammer et al. 2012; R. E. Skelton et al. 2014), plotted in Figure 1 and presented in Table 1. In addition, we find no submillimeter detection in the SCUBA-2 Cosmology Legacy Survey and assume a flux of zero with an error of 1.2 mJy based on the average 1σ depth in the EGS (J. E. Geach et al. 2017). We note that upcoming NOEMA observations (PI: Hviding) of the XRD will provide deeper submillimeter constraints, further placing constraints on the cold dust energy budget.

The source is extremely compact, with an effective radius of $r_e = 0\farcs0322 \pm 0\farcs0042$ in F160W from the A. Van Der Wel et al. (2012) `GALFIT` catalog, where it is flagged as a good fit. Given the F160W point-spread function (PSF) FWHM of $\approx 0\farcs18$, this size is consistent with being unresolved and corresponds to a physical size of $r_e \lesssim 250$ pc. We note that the source appears marginally resolved in the rest-UV ACS imaging (Figure 1), although a detailed morphological analysis would require high signal-to-noise ratio (S/N) rest-UV NIRCam imaging. Extended rest-UV emission may be consistent with similar emission seen in other LRDs that may arise from a host galaxy (e.g., P. Rinaldi et al. 2025; A. Torralba et al. 2026).

2.2. JWST NIRSpec Spectroscopy

The NIRSpec Wide GTO survey (M. V. Maseda et al. 2024) is a 100 hr Cycle 1 program providing shallow low- ($\mathcal{R} \sim 100$) and high-resolution ($\mathcal{R} \sim 2700$) NIRSpec microshutter assembly (MSA) spectroscopy across all five CANDELS fields, with a target selection primarily based on the 3D-HST catalogs. The XRD (3DHST-AEGIS-12014, WIDE-EGS-8949) was targeted with the highest priority (Priority Class 1) because of its high X-ray luminosity. The obtained PRISM, G235H, and G395H spectra have total exposure times of 40, 27, and 29 minutes, respectively. We use the reduced NIRSpec MSA spectra from version 4.4 of the public DAWN JWST Archive (DJA; G. Brammer & F. Valentino 2025), processed with `msaexp` (G. Brammer 2023) following the methodology described in K. E. Heintz et al. (2025) and A. de Graaff et al. (2025a). The 1D spectra were extracted using optimal extraction (K. Horne 1986), with a kernel used to correct for wavelength-dependent slit losses based on the source position.

We show the PRISM spectrum of the XRD in Figure 1 alongside a typical LRD with a strong Balmer break at similar redshift from the RUBIES survey (RUBIES-UDS-144195; A. de Graaff et al. 2025a). We also show the STScI composite quasar template derived from D. E. Vanden Berk et al. (2001) and E. Glikman et al. (2006) as both unobscured and obscured by an SMC dust law (K. D. Gordon et al. 2003). Although the

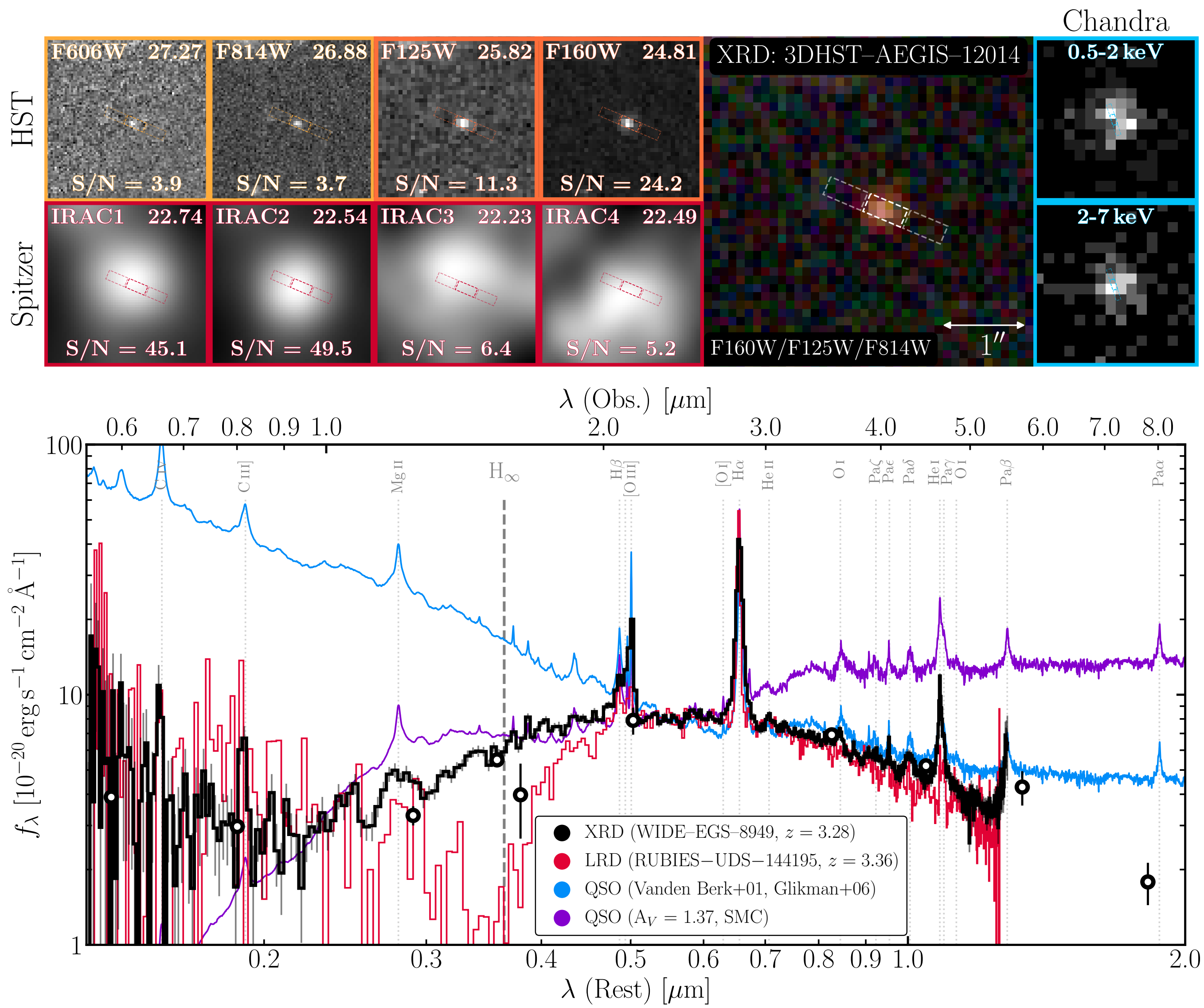

Figure 1. Overview of observations for the XRD. Top panels present the space-based imaging compiled from the 3D-HST survey from HST and Spitzer, the red, green, and blue composite from HST, and the hard and soft X-ray cutouts from Chandra. HST/Spitzer panels show the 4″ × 4″ cutout in the band, magnitude, and S/N, whereas the Chandra panels show 8″ × 8″ cutouts. The bottom panel compares the XRD photometry and scaled NIRSpec/PRISM spectrum (black) to an LRD with a similar rest-optical continuum (RUBIES−UDS−144195; red) and to the STScI composite quasar spectrum derived from D. E. Vanden Berk et al. (2001) and E. Glikman et al. (2006) shown unattenuated (blue) and extincted (purple; $A_V = 1.37$) by an SMC-like dust law (K. D. Gordon et al. 2003). Comparison spectra are normalized to the XRD scaled spectrum at rest 5500 Å.

XRD shares similarities with both populations, such as the red rest-optical continuum of LRDs, it also exhibits distinct differences in its spectral shape and mid-IR properties, which we discuss in detail in Section 3. Comparing the spectrum to the photometry, we find that the PRISM spectrum is a factor of 0.75 fainter. This discrepancy may arise from a combination of factors: (1) the HST-based astrometry may limit the pointing accuracy and hence the applied slit-loss correction, (2) the slit-loss correction itself may carry systematic uncertainties, and (3) given that the source has weak evidence for X-ray variability (Appendix A), we may expect some variability in the rest-UV/optical over the ∼decade time baseline between the HST and JWST observations. We apply this correction throughout this work where noted, but we emphasize that NIRCam observations of this source will be critical to robustly anchor the fluxes.

We perform emission-line fitting using `unite` (R. E. Hviding 2025), which fits the PRISM, G235H, and G395H spectra simultaneously. This approach accounts for the wavelength dependence and undersampling of the line-spread function (LSF) across the different dispersers. We model all emission lines with a narrow component sharing a common width. For permitted transitions, we test additional broad components using Gaussian, Lorentzian, and exponential profiles.

In short, we find clear evidence for broad (FWHM ∼ 2500–3200 km s^{-1}, depending on the assumed line profile) Balmer and Paschen lines (Figure 2). Notably, the broad emission lines are significantly better fit by Lorentzian or exponential profiles compared to a Gaussian profile (see Figure 2 and Appendix B), consistent with the non-Gaussian line profiles observed in LRDs with high-quality spectroscopy (e.g., I. Labbe et al. 2024; A. de Graaff et al. 2025c;

Table 1
X-Ray Dot Measurements

Position		
$z = 3.278$		
$14^{\mathrm{h}}20^{\mathrm{m}}47\overset{\mathrm{s}}{.}498+53°02'32\overset{''}{.}83$		
Photometry		
Band	Flux (μJy)	Error (μJy)
HST ACS F606W	0.044	0.011
HST ACS F814W	0.064	0.017
HST WFC3 F125W	0.169	0.015
HST WFC3 F160W	0.430	0.018
CFHT WIRCam J	−0.043	0.093
CFHT WIRCam H	0.35	0.12
CFHT WIRCam K_s	1.22	0.15
Spitzer IRAC Ch. 1	2.885	0.064
Spitzer IRAC Ch. 2	3.477	0.070
Spitzer IRAC Ch. 3	4.62	0.72
Spitzer IRAC Ch. 4	3.62	0.70
Spitzer MIPS 24 μm	4.4	5.1
X-Ray Analysis		
Parameter	Measurement	Error
Exposure time (s)	7.729×10^5	⋯
Aperture counts (counts)	205.0	14.2
Background counts (counts)	15.818	0.460
Net counts (counts)	189.182	14.325
Rate (0.5−7 keV) (counts s^{-1})	2.46×10^{-4}	0.19×10^{-4}
$f_{0.5-7\,\mathrm{keV}}$ (erg s^{-1} cm^{-2})	2.7×10^{-15}	0.2×10^{-15}
Power-law Index (Γ)	1.8	0.2
N_{H} (XRD) (cm^{-2})	2.4×10^{22}	2.0×10^{22}
$L_{2-10\,\mathrm{keV}}$ (Int.) (erg s^{-1})	1.51×10^{44}	0.24×10^{44}
Cash statistic (dof = 441)	321.3	⋯

V. Rusakov et al. 2026; A. Torralba et al. 2026). Appendix B further details the model used and also provides the recovered fluxes, rest equivalent widths (EWs), and kinematics.

2.3. X-Ray Data

XDEEP2 (A. D. Goulding et al. 2012) provides Chandra ACIS data from which this source's spectrum was extracted. We stack the multiepoch data and perform a basic spectral fitting in XSPEC (K. A. Arnaud 1996) using an attenuated power-law model accounting for foreground Milky Way absorption. The X-ray spectral analysis reveals a rather typical AGN X-ray spectrum: an intrinsic rest-frame 2–10 keV luminosity of $\sim 10^{44}$ erg s^{-1} with a typical intrinsic power-law slope of $\Gamma = 1.8$ and moderate attenuation $N_{\mathrm{H}} \sim 10^{22}$ cm^{-2}. This places the source near the conventional boundary between unobscured (type 1) and obscured (type 2) X-ray AGN (R. C. Hickox & D. M. Alexander 2018). This high luminosity, combined with moderate evidence for X-ray variability (see Appendix A), unambiguously identifies the source as an AGN (W. N. Brandt & D. M. Alexander 2015). We compare the X-ray scaling relationships of the XRD to other AGN and LRD populations in Figure 3, which we discuss in detail in Section 3. Results from the XSPEC X-ray analysis are provided in Table 1, whereas additional details of the X-ray data and analysis are provided in Appendix A.

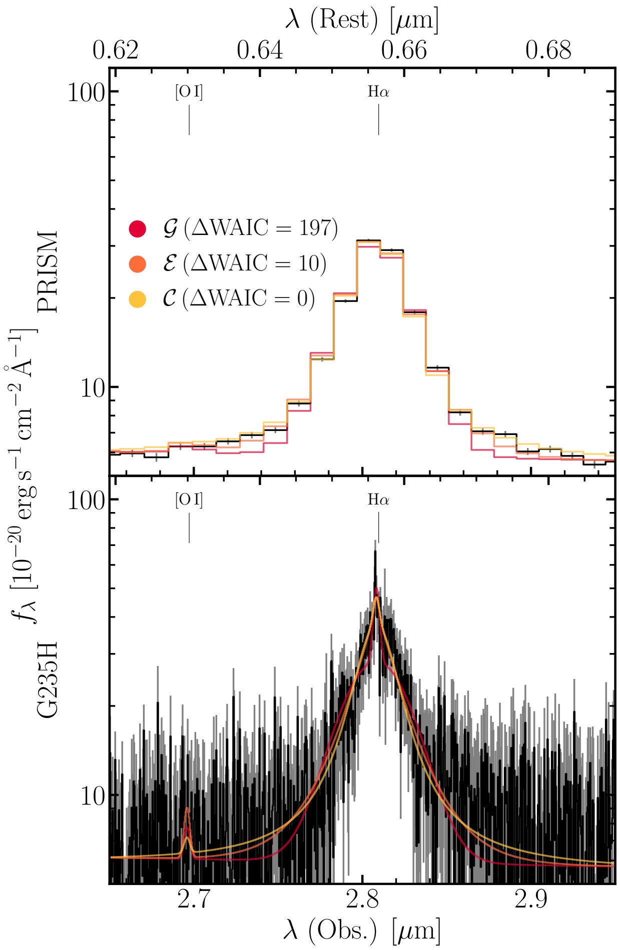

Figure 2. Zoom-in on the Hα emission line in the PRISM (top) and G235H (bottom) spectra. The observed data are shown in black, with 1σ uncertainties in gray. We overplot the best-fit `unite` models using a Gaussian narrow plus different broad-line profiles: Gaussian (red), exponential (orange), and Lorentzian (yellow). The fit strongly prefers exponential and Lorentzian profiles, suggesting extended wings.

3. A Dust-reddened AGN?

The XRD has unambiguous signatures of SMBH accretion, exhibiting both a high X-ray luminosity ($L_{2-10\,\mathrm{keV}} \sim 10^{44}$ erg s^{-1}) and broad Balmer emission lines (FWHM $\sim$ 2700–3200 km s^{-1}). In further, albeit tentative, support of a typical AGN origin, the rest-UV spectrum reveals emission from C IV and C III], detected at 2.3σ and 6.2σ significance with measured EWs of 25 and 43 Å, respectively (Table B1). Such high-ionization lines are typically observed in AGN but are rare in LRDs with a few notable exceptions (e.g., H. B. Akins et al. 2025; I. Labbe et al. 2024). Although C III] emission can originate from star formation, significant C IV is challenging to produce via stellar photoionization processes alone (M. Hirschmann et al. 2019), potentially favoring an AGN origin despite the modest significance of the detection. We also search for Mg II, but the line falls at the minimum of the PRISM's wavelength-dependent resolution, precluding a robust detection.

However, other features of the XRD appear remarkably LRD-like and distinct from typical dust-obscured quasars

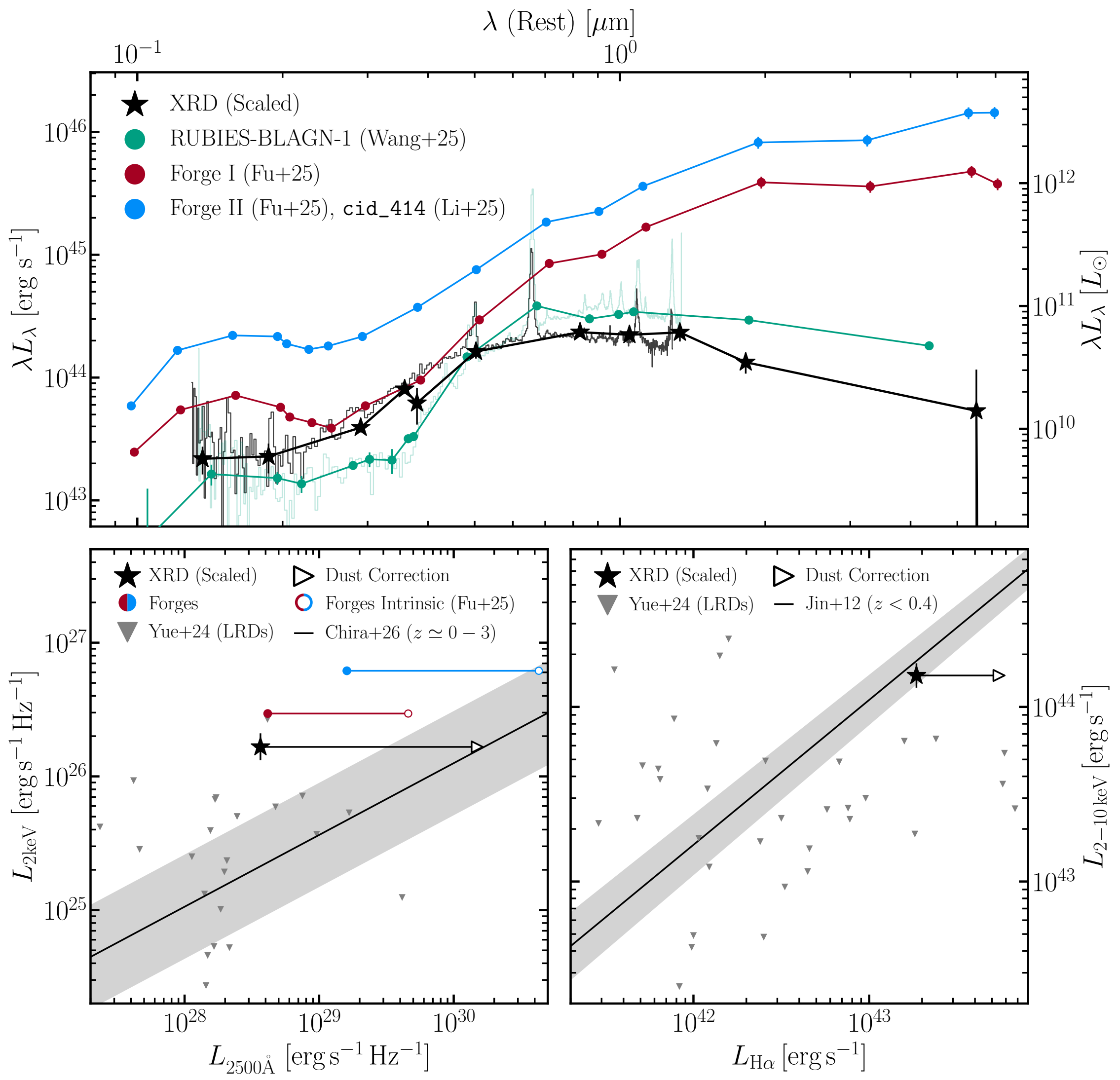

Figure 3. Top: the rest-frame SED of the XRD (black) compared to RUBIES-BLAGN-1 (green; B. Wang et al. 2025) and Forge I and II (`cid_414`; red and blue, respectively; S. Fu et al. 2025; Z.-J. Li et al. 2025). Bottom Left: $L_{2,\rm keV}$ vs. $L_{2500 Å}$ for the XRD, the Forges, and the X-ray upper limits for LRD nondetections from M. Yue et al. (2024; gray triangles). The XRD and Forge sources lie well above the standard $z \simeq 0$–3 AGN relation (M. Chira et al. 2026), indicating that they are X-ray luminous for their UV emission. Applying a dust correction (Section 3.3) to the XRD, along with the corrections for the Forges in S. Fu et al. (2025), brings all three sources closer to the relation. Bottom right: comparison of X-ray and Hα luminosity. The measured XRD properties follow the relation for $z < 0.4$ unobscured AGN (C. Jin et al. 2012), but correcting the Hα luminosity for dust in the same manner as $L_{2500\,Å}$ produces an Hα luminosity that is overluminous for its X-ray emission.

(Figure 1). Specifically, the XRD has blue mid-IR colors indicative of a falling continuum, which differs from obscured quasars that typically show enhanced mid-IR emission from a hot dust torus. Instead, the XRD shares the steep red rest-optical continuum characteristic of LRDs, though its spectral inflection point occurs blueward of the Balmer limit (∼2000 Å), unlike typical LRDs (D. J. Setton et al. 2025; A. de Graaff et al. 2025b).

Nevertheless, the X-ray luminosity stands in stark contrast to its comparatively weak rest-UV emission, indicating that the central AGN engine must be subject to significant obscuration. In this section we aim to assess whether the XRD can be explained as a dust-reddened AGN. We first place the XRD in the context of empirical X-ray scaling relationships. We then test whether a dust-reddened AGN model can reproduce the broadband SED and the rest-optical spectrum, without violating the X-ray observations, mid-IR constraints, or typical dust laws for galaxies and AGN.

3.1. X-Ray Scaling Relationships

In the bottom half of Figure 3, we compare the XRD's intrinsic (i.e., absorption-corrected) X-ray properties to standard AGN scaling relationships. The XRD is significantly more X-ray luminous than the upper limits for LRDs (M. Yue et al. 2024), and its X-ray luminosity is therefore comparable to that of the "Forges" objects (S. Fu et al. 2025) that were recently proposed to be transitionary sources between LRDs and quasars. Unlike the Forges, however, the XRD lacks the mid-IR rise attributed to dust emission seen for those sources.

All three sources lie above the standard $L_{\rm X}$−$L_{\rm UV}$ relation (M. Chira et al. 2026), indicating that they are remarkably X-ray luminous given their observed UV emission. Applying a dust correction based on spectral continuum fitting (Section 3.3) to the UV luminosity would bring the source onto this relation, but applying the same correction to the Hα luminosity would move it below the $L_{\rm X}$−$L_{\rm H\alpha}$ relation for

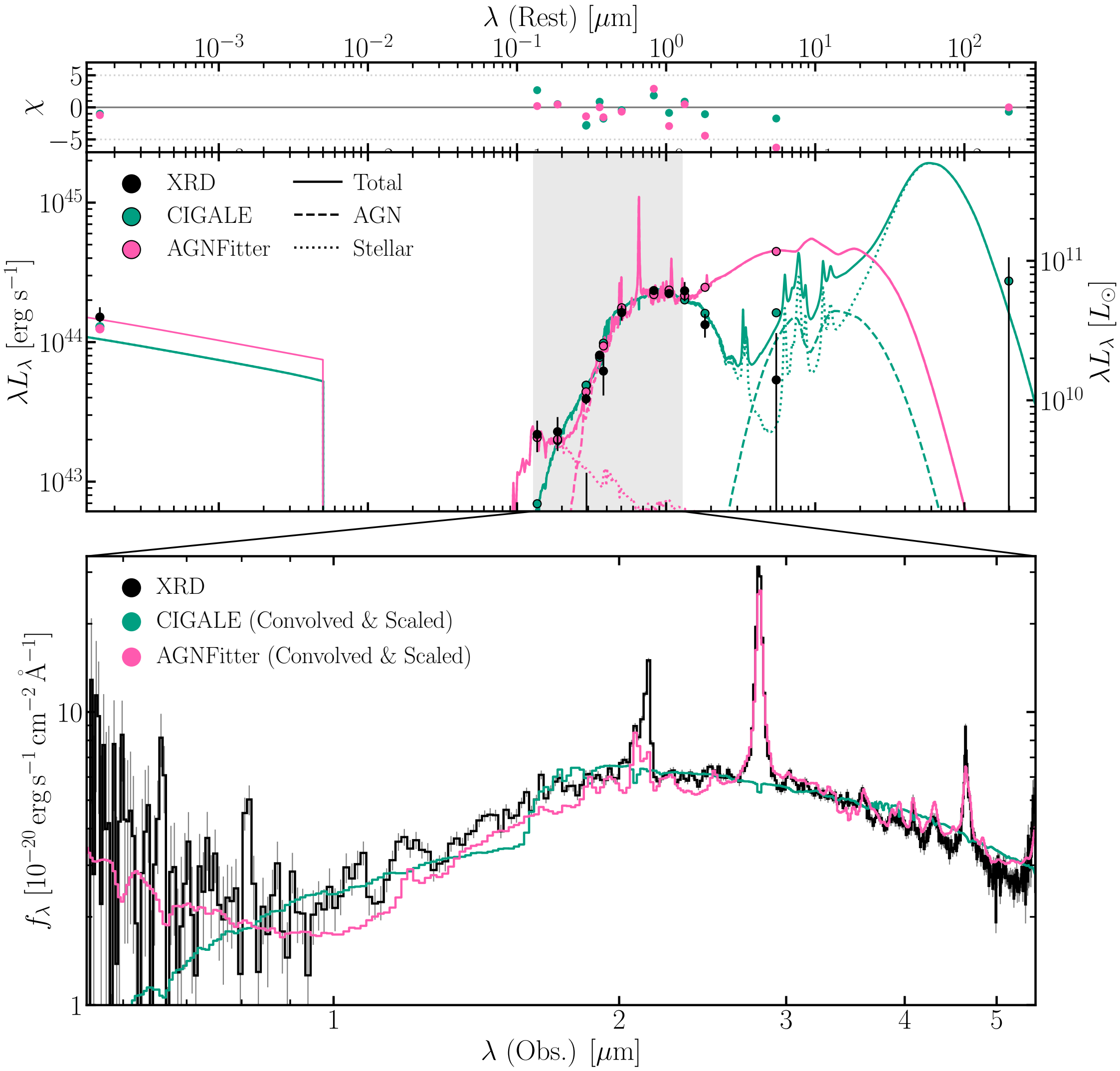

Figure 4. X-ray through submillimeter SED fitting of the XRD with both CIGALE (green) and AGNFitter (pink). The top panel shows the best fits (solid) decomposed into their AGN (dashed) and stellar (dotted) components, along with the scaled residuals. The bottom panel compares the models, scaled and convolved to the PRISM resolution, to the PRISM spectrum; note that the models are not fit to the spectral data. In order to explain the X-ray luminosity, both models require a strong AGN component. However, to minimize discrepancy with the relatively weak mid-IR flux, CIGALE heavily obscures the AGN component, requiring an evolved stellar population to dominate in the rest-optical, inconsistent with the spectrum. AGNFitter, on the other hand, is able to fit the rest-optical spectrum with an AGN, but it substantially overpredicts in the mid-IR.

unobscured AGN (C. Jin et al. 2012), which it currently follows. This tension implies either that the broad-line and continuum regions are subject to different levels of obscuration (i.e., the broad-line region is less obscured) or that these high-redshift sources deviate from local scaling relationships, which are themselves susceptible to selection effects and intrinsic scatter.

It is also instructive to compare the XRD's bolometric output to its intrinsic X-ray luminosity: $k_X \equiv L_{\rm bol}/L_{2-10\,\rm keV}$. We integrate our submillimeter through X-ray observations to estimate $L_{\rm bol} \simeq 5 \times 10^{44}$ erg s^{-1}, implying $k_X \simeq 3.3$. Alternatively, we can infer $L_{\rm bol}$ from the Hα luminosity using empirical scalings: adopting a canonical J. E. Greene & L. C. Ho (2005) calibration gives $k_X \simeq 18$, whereas adopting the LRD motivated calibration from J. E. Greene et al. (2026) gives $k_X \simeq 2.1$. The latter is much closer to the direct SED-based estimate, and together these estimates suggest that the XRD is X-ray bright for its bolometric output when compared to typical AGN at similar luminosities (Figure 4: F. Duras et al. 2020), the opposite of what is observed in some high-z samples, which are typically X-ray weak (e.g., R. Maiolino et al. 2025).

3.2. SED Fitting

We use two SED fitting routines to test across AGN model implementations: CIGALE (D. Burgarella et al. 2005; S. Noll et al. 2009; M. Boquien et al. 2019; G. Yang et al. 2020) and AGNFitter (G. Calistro Rivera et al. 2016; L. N. Martínez-Ramírez et al. 2024). Both models are fit using only the photometry described in Section 2.1, as well as the X-ray constraints on $L_{2-10\,\rm keV}$ and Γ detailed in Section 2.3. The full SED models are shown in Figure 4 and are decomposed into their respective stellar and AGN components. In addition, by convolving the model with the wavelength-dependent LSF of the PRISM and multiplying the models by the measured spectroscopic scale factor, we also compare the predicted model SED to the NIRSpec spectrum, although we stress that the spectrum was not used in the fitting itself.

We adopt this photometry-only approach to keep the SED constraints focused on the broadband energy budget and the implied X-ray-to-mid-IR scaling relations, rather than on achieving an optimal fit to the densely sampled rest-optical continuum in the PRISM data. Including the spectrum directly in the likelihood would strongly up-weight the rest-optical regime relative to the sparsely sampled mid-IR and X-ray constraints, potentially driving the fit toward models that reproduce the detailed continuum shape, although they fail to satisfy the global SED properties. We therefore use the spectrum as an external consistency check on the SED models and perform dedicated spectral modeling in Section 3.3.

3.2.1. CIGALE

CIGALE is able to model the XRD photometry from the X-ray through the submillimeter and is designed to account for the energy balance for any dust-attenuated stellar components. We use CIGALE with the I. E. López et al. (2024) X-ray prescription, which implements the L_X–$L_{12\,\mu\mathrm{m}}$ scaling relationship from P. Gandhi et al. (2009), alongside the SKIRTOR (M. Stalevski et al. 2012, 2016) AGN models. Briefly, for the galaxy component we use a delayed-τ star formation history, the G. Bruzual & S. Charlot (2003) stellar population models, the D. Calzetti et al. (2000) dust attenuation law, and the THEMIS (A. P. Jones et al. 2017) dust emission prescription. We provide the full details and results of our CIGALE SED fitting in Appendix C and Table C1.

The best-fitting CIGALE model (Figure 4) explains the red rest-optical continuum as dominated by an older stellar component ($t_{\mathrm{age}} \sim 1$ Gyr; $M_\star \sim 2.5 \times 10^{10} M_\odot$) that is moderately dust attenuated ($A_V \sim 0.5$). However, to maintain the P. Gandhi et al. (2009) scaling relationships between the X-ray and mid-IR, the model heavily suppresses the AGN contribution in the optical through mid-IR with a torus with a high covering fraction ($\theta_{\mathrm{open}} \approx 55°$–$85°$; $\theta_{\mathrm{open}} = 90°$ is unity covering fraction) with a direct view through the torus ($i \approx 50°$–$90°$; $i = 0°$ is face-on). The resulting torus geometry effectively hides the hot dust components at the inner torus radii, preventing the significant mid-IR emission. Although this produces a good fit to the photometry, the resulting stellar-dominated model is strongly in tension with the PRISM spectrum owing to the lack of a 4000 Å break and emission lines.

3.2.2. AGNFitter

AGNFitter is primarily designed for fitting the SED of AGN and is well suited for measuring AGN properties and determining the level of obscuration. It achieves this by decomposing the SED into four physical components: an accretion disk, a hot dust torus, a stellar population, and cold dust in star-forming regions. We utilize the M. J. Temple et al. (2021) accretion disk models, SKIRTOR torus models, G. Bruzual & S. Charlot (2003) stellar population models, and C. Schreiber et al. (2017) starburst models. The X-ray emission is linked to the mid-IR (6 μm) luminosity using the relation from D. Stern (2015).

As shown in Figure 4, AGNFitter is able to reproduce the red optical continuum with a reddened AGN component. In particular, the fit reproduces the PRISM spectroscopy quite accurately, including the strength of most hydrogen emission lines, without being fit directly to these data. However, the model predicts a significant hot dust torus component in the mid-IR to maintain the X-ray-to-mid-IR relation. This predicted mid-IR emission significantly exceeds the observed Spitzer fluxes, with a 4.4σ and 6.2σ discrepancy in IRAC Channel 4 and MIPS 24μm, respectively (combined 7.6σ), indicating that the reddening mechanism in the XRD does not produce the expected thermal reemission associated with a wide grid of torus models. We provide the full details and results of our AGNFitter SED fitting in Appendix C.

3.3. Spectral Continuum Fitting

The SED fitting analysis indicates that if the XRD is a dust-reddened AGN, its dust properties fall outside of the parameter range considered in standard SED fitting codes. We therefore also follow the empirical approach of Y. Ma et al. (2025a), to determine which extinction law would be needed in order to explain the XRD as a reddened, intrinsically UV-luminous AGN. We adopt the double power-law AGN continuum model from M. J. Temple et al. (2021) as the intrinsic spectrum. This intrinsic continuum is then attenuated using the flexible attenuation law of S. Noll et al. (2009), which allows for a variable slope and extinction. We also include an unattenuated reflection component to account for the UV upturn in the spectrum. We fit this model to the PRISM spectrum, masking out the regions around strong emission lines (Hβ, [O III], Hα, and Paβ).

The best-fit model, shown in Figure 5, provides a good description of the rest-UV–optical continuum spectrum ($\chi^2_\nu = 2.53$). However, this fit requires a high extinction of $A_V \sim 1.8$ mag and an extremely steep extinction curve. Following A. de Graaff et al. (2025c), we quantify the steepness of the attenuation curve using the optical slope, defined as the ratio of the attenuation at 3500 and 5500 Å (A_{3500}/A_{5500}). As shown in the right panel of Figure 5, the required optical slope for the XRD is substantially steeper than standard laws for the Milky Way, LMC, SMC, and typical galaxy populations (D. Calzetti et al. 2000; K. D. Gordon et al. 2003). It is also significantly steeper than the average extinction curves derived for AGN (e.g., R. Maiolino et al. 2001; B. Czerny et al. 2004; C. M. Gaskell et al. 2004), which are typically shallower than the SMC law.

Such a combination of a steep optical slope and high attenuation is physically difficult to explain with dust; that is, systems with more extinction typically exhibit grayer attenuation curves. Although AGN with extreme attenuation curves are known, they are typically found in the rare iron low-ionization broad absorption line quasar (FeLoBALQ) population, which, unlike the XRD, exhibit broad UV absorption lines, show high X-ray column densities, and still show mid-IR excesses (K. M. Leighly et al. 2014; C. M. Krawczyk et al. 2015; K. M. Leighly et al. 2025). Therefore, the location of the XRD in this parameter space of high A_V and steep slope is therefore highly unusual and potentially inconsistent with a dust screen scenario.

The Balmer decrement (Hα/Hβ) provides an independent constraint on whether the red continuum can be explained by dust extinction. For our statistically preferred broad-line profile models (Lorentzian and exponential), the narrow-line Balmer decrement is consistent with case B recombination within the uncertainties (Table B1), suggesting little reddening in the narrow-line region and/or host galaxy. In contrast, the measured broad-line decrement (9.5 ± 0.5) is strongly elevated, potentially indicative of heavy nuclear dust

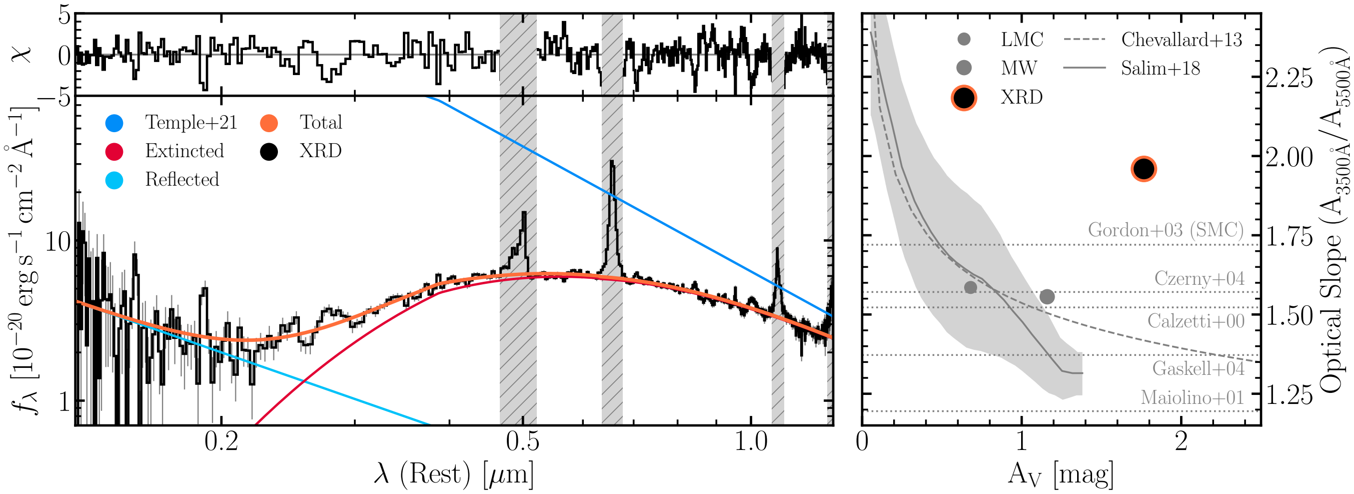

Figure 5. Following the approach of Y. Ma et al. (2025a), we attempt to model the PRISM spectrum of the LRD assuming that it is dominated by a dust-extincted, intrinsically UV-luminous AGN. We attenuate the M. J. Temple et al. (2021) AGN–power-law continuum using a flexible S. Noll et al. (2009) attenuation law plus an unattenuated reflection component. The left panel shows the best-fit attenuated AGN model (orange) decomposed into the intrinsic (blue), reflected (cyan), and extincted (red) components. The right panel compares the derived extinction parameters to typical galaxy populations (J. Chevallard et al. 2013; S. Salim et al. 2018), the LMC and Milky Way (K. D. Gordon et al. 2003), standard dust laws (D. Calzetti et al. 2000; K. D. Gordon et al. 2003), and averages from local AGN populations (R. Maiolino et al. 2001; B. Czerny et al. 2004; C. M. Gaskell et al. 2004).

obscuration. However, estimating a dust extinction from this value is not straightforward, as intrinsic broad-line Balmer decrements are not expected to follow case B: local unobscured AGN often show enhanced intrinsic broad-line decrements up to 4.2 (X. Dong et al. 2008), with models predicting values up to ∼5 (K. T. Korista & M. R. Goad 2004), plausibly due to high gas densities and optical depth effects. Thus, while the intrinsic baseline is uncertain, the elevated broad-line decrement remains formally consistent with a nuclear dust obscuration scenario.

Nevertheless, these discrepancies, namely the extreme dust properties required to explain the reddened rest-optical yet weak mid-IR emission, mirror the arguments presented in Y. Ma et al. (2025a) and A. de Graaff et al. (2025c) against a pure dust interpretation for LRDs.

4. Gas-dominated Reddening?

The high X-ray intrinsic luminosity of the XRD ($L_{2-10\,\mathrm{keV}} \sim 10^{44}\,\mathrm{erg\,s^{-1}}$) at face value implies a correspondingly high intrinsic UV luminosity. As demonstrated in Section 3, typical dust attenuation scenarios fail to reconcile this intrinsic emission with the observed red rest-optical continuum without invoking extreme dust properties. We therefore explore the alternative scenario proposed for the LRD population: that the intrinsic UV continuum is reddened by dense, optically thick gas (e.g., A. de Graaff et al. 2025c; K. Inayoshi & R. Maiolino 2025; X. Ji et al. 2025; D. Kido et al. 2025; R. P. Naidu et al. 2025).

4.1. The XRD in Context of the LRD Population

Following A. de Graaff et al. (2025b), we decompose the PRISM spectrum into a modified blackbody ($f_\nu \propto \nu^\beta B_\nu$, or equivalently $f_\lambda \propto \lambda^{-\beta} B_\lambda$) representing the thermalized gas emission and a power law to reproduce the UV ($f_\lambda \propto \lambda^\beta$). This simple model provides an excellent description of the XRD's spectral shape ($T_{\mathrm{eff}} \simeq 6400$ K; $\beta \simeq -1$), capturing both the steep red continuum and the UV upturn. However, the derived $\beta_{\mathrm{BB}} = -1$ indicates a continuum shape that is broader than a single-temperature blackbody, which, although consistent with typical LRDs, argues against the emission arising from a single, purely thermal component.

We compare the XRD's modified blackbody parameters and emission-line EWs and luminosities with the sample of LRDs and broad-line AGN from A. de Graaff et al. (2025b) and R. E. Hviding et al. (2025) in Figure 6 (for reference, the modified blackbody decomposition is shown in Figure 7). Regardless of the assumed broad-line profile (Gaussian, Lorentzian, or exponential), the XRD consistently falls within the region traced by the LRD population (A. de Graaff et al. 2025b).

Specifically, the XRD exhibits an extreme Balmer decrement (Hα/Hβ ∼ 10; Figure 6, top middle), comparable to that seen in the LRD population (A. de Graaff et al. 2025b) and consistent with originating from dense gas environments (Z. Yan et al. 2025). It also has a very large Hα EW ($\mathrm{EW}_{\mathrm{H}\alpha}$ ∼ 550–620 Å) and is unusually Hα luminous for its absolute UV magnitude, lying even farther from the standard AGN relation than the typical LRDs (Figure 6, right). Moreover, we detect strong O I λ8446 (Table B1) emission that follows the $L_{\mathrm{H}\alpha}$–L_{OI} scaling relation in A. de Graaff et al. (2025b), implying high-density, optically thick gas (Figure 6, bottom middle). Finally, the XRD tracks LRD-specific trends such as the correlation between Hα luminosity and blackbody luminosity, further supporting its association with the gas-enshrouded LRD class (Figure 6, bottom left).

4.2. A Late-stage LRD?

The fact that the UV−optical spectral properties of the XRD closely resemble those of the LRD population raises major questions regarding the physical conditions of the gas surrounding the central engine. Recent efforts to model LRDs (e.g., A. de Graaff et al. 2025c; X. Ji et al. 2025; H. Liu et al. 2025; R. P. Naidu et al. 2025; A. J. Taylor et al. 2025) all invoke a dense gas envelope that is Compton thick, forming a key argument in explaining their observed X-ray weakness. Moreover, these models give rise to a dominant thermal component in the rest-frame optical, well approximated by a ∼5000 K blackbody (A. de Graaff et al. 2025b; H. Umeda et al. 2026),

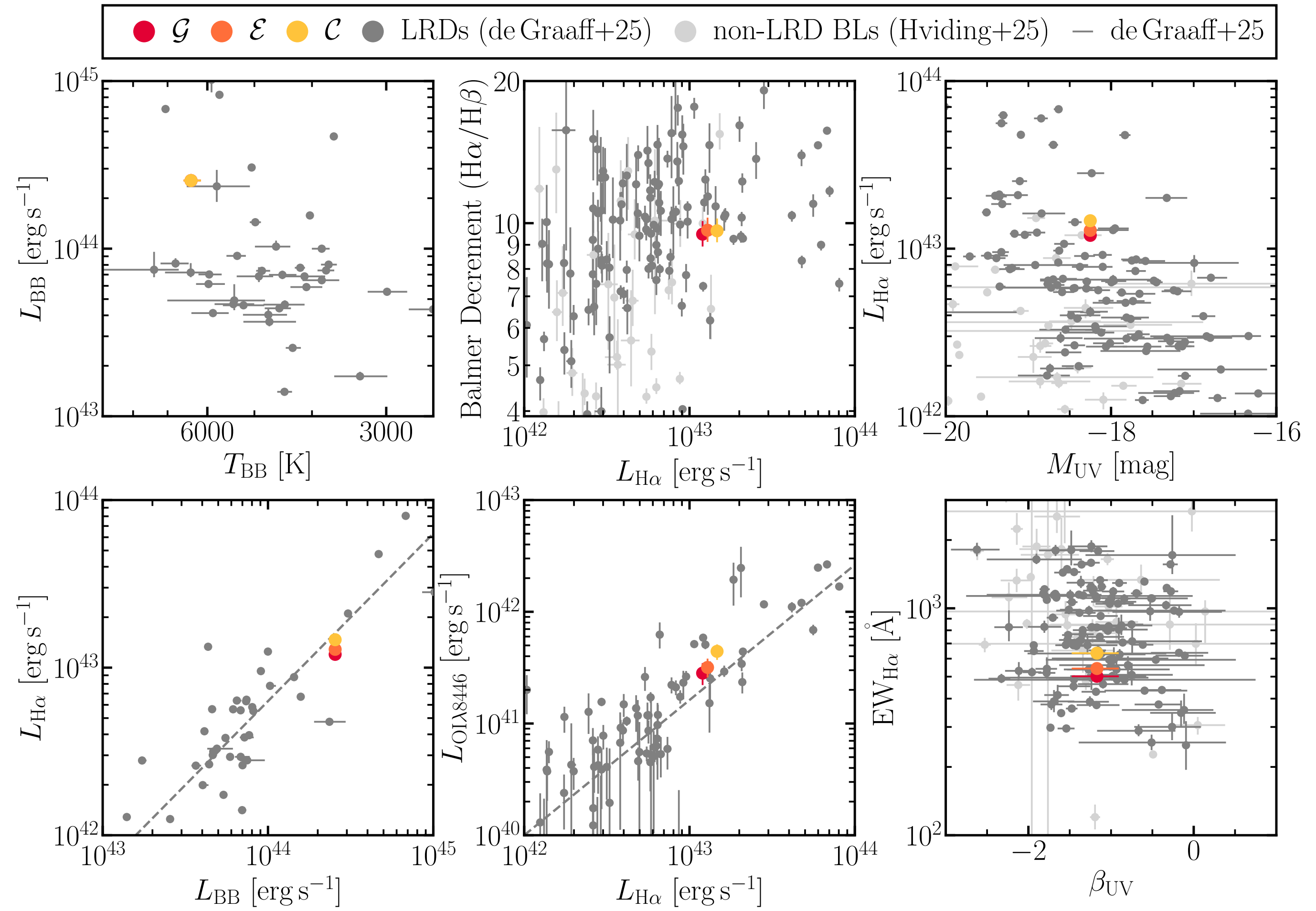

Figure 6. Comparison of the XRD to the population of LRDs (dark gray) and non-LRD broad-line objects (light gray) from A. de Graaff et al. (2025b) based on emission-line and modified blackbody fitting. Colors correspond to the assumed line profile of the broad component: red for Gaussian, orange for exponential, and yellow for Lorentzian. Top left: blackbody temperature vs. luminosity; top middle: Balmer decrement vs. Hα luminosity; top right: Hα luminosity vs. UV magnitude; bottom left: Hα luminosity vs. blackbody luminosity; bottom middle: O I λ8446 luminosity vs. Hα luminosity; bottom right: Hα EW vs. UV power-law slope. The XRD generally lies in regions occupied by LRDs, apart from not non-LRD broad-line galaxies, and on the relations derived in A. de Graaff et al. (2025b).

while simultaneously producing strong Balmer breaks and high intrinsic Balmer decrements.

The XRD differs from these models in three key respects: it is X-ray luminous, its UV−optical SED is broader than a single thermal component, and its continuum turnover occurs blueward of the Balmer limit. Motivated by this, we explore whether a dense envelope can still dominate the observed UV −optical emission while permitting X-rays to escape. We adopt a patchy, multiphase gas envelope with a subunity covering fraction, which can be physically interpreted as a dynamically unstable, transitional configuration. In this picture, optically thick regions thermalize and shape the UV −optical spectrum, whereas optically thin channels provide direct sight lines to the compact X-ray source.

In such a transitional, anisotropically clearing geometry, the relatively modest $T_{\rm eff} \sim$ 5000–7000 K inferred for the reprocessed continuum can be understood as an effective photospheric temperature of the dominant reprocessing layer: a Compton-thin line-of-sight column does not preclude substantial reprocessing at other angles or larger radii, and as the envelope disperses, the photosphere may recede such that the color temperature evolves only weakly. We note, however, that recent work suggests that hotter ($T_{\rm eff} \sim 10^4$ K) phases may naturally arise once the envelope becomes unstable or begins to disperse (e.g., D. Kido et al. 2025), highlighting that dedicated radiative-hydrodynamic modeling will be needed to predict the time-dependent temperature evolution. Although idealized, such a short-lived phase could plausibly be observed given the abundance of LRDs ($\sim$0.5 arcmin^{-2}; V. Kokorev et al. 2024) and their small inferred lifetimes ($\sim$10 Myr; A. D. Santarelli et al. 2026; M. C. Begelman & J. Dexter 2026).

Although idealized, such a short-lived phase could plausibly be observed given the abundance of LRDs ($\sim$0.5 arcmin^{-2}; V. Kokorev et al. 2024) and their small inferred lifetimes ($\sim$10 Myr; A. D. Santarelli et al. 2026; M. C. Begelman & J. Dexter 2026).

To explore the properties of such an envelope, we use the theoretical spectral templates of H. Liu et al. (2026), which update the models in H. Liu et al. (2025). Emission features of the model spectra are mainly determined by the effective temperature and the atmosphere density, the latter parameterized by log(g). The spectral similarities between the XRD and LRDs motivate us to start from a single template of $T_{\rm eff}$ = 5000 K and log(g) = −2.0 that well describes the optical–to–near-IR SED of LRDs such as UNCOVER-45924 (I. Labbe et al. 2024). However, this model fails to fit the XRD continuum, producing an overly narrow and red SED. This calls for an additional, bluer emission component, as already

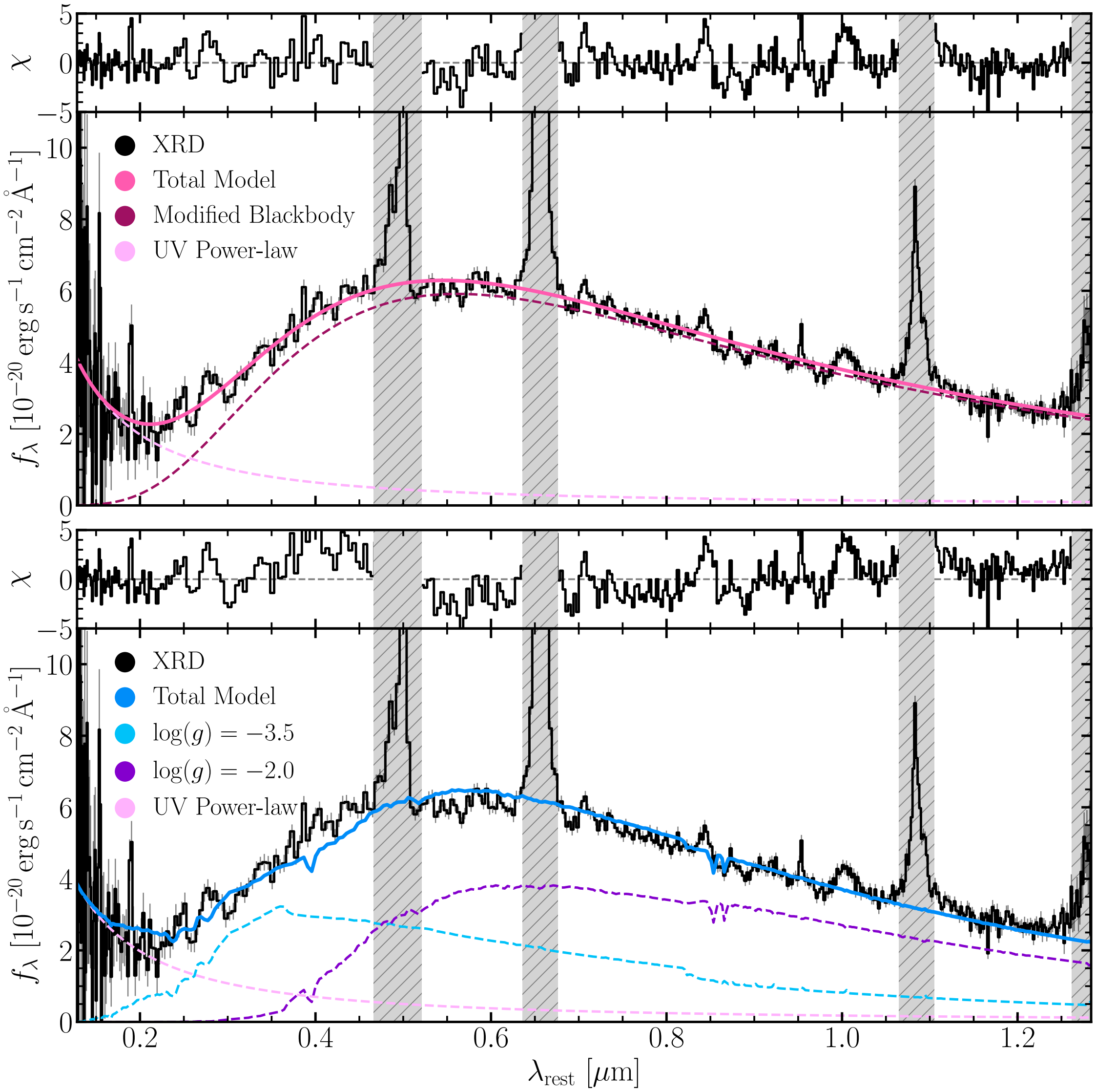

Figure 7. Modeling the XRD continuum as emission from a dense gas envelope. Top: following A. de Graaff et al. (2025b), we perform a phenomenological fit decomposing the spectrum into a modified blackbody (magenta dashed), representing the thermalized gas emission, and a UV power law (pink dashed). This simple model provides an excellent description of the continuum of the XRD. Bottom: a physical fit (blue) combining two $T_{\rm eff} = 5000$ K low-density gas atmosphere models with different densities, $\log(g) = -3.5$ (cyan dashed) and $\log(g) = -2.0$ (purple dashed), that are attenuated by SMC dust ($A_V \sim 0.6$) plus a UV power law (pink dashed). The residuals for both fits are shown in the upper subpanels.

suggested by the high $T_{\rm eff}$ and $\beta_{\rm BB} \sim -1$ in our modified blackbody fit.

We then test whether a hotter component could provide the required blue emission by adding templates with higher $T_{\rm eff}$ at comparable or higher $\log(g)$. However, these models introduce a pronounced Balmer break that is not present in the NIRSpec/PRISM spectrum. We instead vary the atmosphere density: lower-$\log(g)$ templates naturally produce bluer continua without invoking higher temperatures. In Figure 7 (bottom), a combination of two $T_{\rm eff} = 5000$ K components at different densities ($\log(g) = -3.5$ and $\log(g) = -2.0$) reproduces the broad, blue rest-optical SED while maintaining a weak Balmer break, after attenuation by moderate SMC-like dust ($A_V \sim 0.6$). We invoke an unattenuated power law to produce the rest-UV that could arise from the host galaxy, an AGN accretion disk, or a combination of both.

We interpret this fit as evidence for a patchy, multiphase gas envelope surrounding the black hole. In this picture, the blue emission and suppressed Balmer break in the low-density component ($\log(g) = -3.5$) are a consequence of scattering-dominated radiative transfer. We caution, however, that the solution requires fine-tuning the density to avoid an inverse Balmer break and still necessitates some dust attenuation. Moreover, the H. Liu et al. (in preparation) framework assumes an optically thick medium ($\tau \gg 1$) and may therefore not capture the true physical state of the XRD if it is transitioning between optically thick and optically thin. Nevertheless, this exercise highlights that the dense, optically thick atmosphere conditions inferred for typical LRDs (where the model assumptions are more likely to be valid) struggle to reproduce the XRD SED, pointing to lower densities as a potential path forward.

Finally, we note that S. Fu et al. (2025) recently proposed a similar qualitative picture for the Forges, two X-ray-luminous, compact red sources. However, the XRD differs from these objects in important ways: we do not find evidence for hot dust out to rest-frame 5 μm (Figure 3), the optical luminosity is comparable to that of typical LRDs, and the host galaxy is faint. Therefore, if truly reddened by gas rather than dust, the XRD offers a crucially different scenario for the late-stage phase of LRDs.

5. Summary and Discussion

The XRD presents a unique set of properties that challenge standard classification. Although its high X-ray luminosity ($L_{2-10\,\mathrm{keV}} \gtrsim 10^{44}\,\mathrm{erg\,s^{-1}}$) and spectral shape ($\Gamma \sim 1.8$) would normally unambiguously identify it as a typical AGN, it shares striking similarities with the LRD population. Specifically, it exhibits a V-shaped spectral continuum with blackbody-like emission, non-Gaussian broad lines with significant wings, and weak mid-IR emission in conflict with the existence of a hot dust torus. However, a key distinction in the UV−optical SED remains: the spectral inflection point lies blueward of the Balmer limit, rather than at or redward of the Balmer limit as is typical of LRDs (A. de Graaff et al. 2025b).

We have systematically explored whether the properties of the XRD can be explained by dust obscuration. However, standard dust models fail to reproduce the observed SED without invoking a combination of extremely steep attenuation curves at high dust extinction that are inconsistent with those observed in local galaxies or AGN. Dust-obscured AGN models also require hot dust components that are incompatible with the observed Spitzer photometry based on typical AGN scaling relations. Although hot-dust-deficient quasars have been observed in X-ray AGN surveys (H. Hao et al. 2010), they are typically UV-luminous. The fact that the narrow-line Balmer decrement is consistent with case B recombination implies that the obscuration is primarily nuclear. This would necessitate a nuclear dust component, which typically produces strong hot dust emission, and is therefore in tension with the absence of IR emission in a hot-dust-deficient quasar interpretation. Although we cannot strictly rule out exotic dust scenarios for this single source without further data, for these reasons we do not prefer attributing the XRD's properties to a dust-obscured AGN.

Alternatively, we attempt to describe the continuum as arising from a dense gas envelope, consistent with the black hole star scenario proposed for LRDs. We find that such a gas-reddened model can approximately reproduce the correct spectral shape, but it requires fine-tuning the densities of at least two optically thick components. This suggests that the XRD may reside in a physical regime not well captured by current static atmosphere models that assume high optical depths ($\tau \gg 1$). The XRD may therefore represent an object in transition, where the gas envelope is multiphase and the optical depth is intermediate between the optically thick limit of atmospheric models and the optically thin limit of photoionization codes like `cloudy` (C. M. Gunasekera et al. 2025). Nevertheless, it remains a challenge to envision a configuration in which the optical emission is still dominated by an optically thick envelope while allowing optically thin sight lines to the compact X-ray source, yet simultaneously preventing UV emission from leaking out from the accretion disk. This tension could be resolved by moving from spherical symmetry to nonspherical or clumpy geometries that allow direct views of the X-ray corona while maintaining high reprocessing of the accretion disk emission. However, keeping the envelope at $T \sim 6000\,\mathrm{K}$ despite emerging Compton-thin sight lines may also be difficult since the temperature of the envelope may be expected to exceed $\sim 10^4$ K as it disperses (D. Kido et al. 2025).

If the XRD is indeed an object in transition, it offers a unique laboratory to study the nature of LRDs. Future observations will be critical to test this hypothesis. JWST/MIRI spectroscopy and imaging are therefore crucial to characterize the mid-IR dust emission and to determine whether a hidden hot dust component exists, whereas upcoming NOEMA observations (PI: Hviding) will constrain the cold dust budget. Although tentative X-ray variability supports the transitional hypothesis, continued X-ray monitoring is required to confirm this, whereas NIRCam imaging would provide constraints on any long-term rest-optical changes.

Crucially, if the rest-optical continua of LRDs are indeed dominated by dense, optically thick gas envelopes and the Balmer emission lines are broadened primarily by scattering processes, as opposed to gravitational motions, then there remain no direct pieces of observational evidence that the luminosities of LRDs are powered by accretion onto an SMBH. Confirming the XRD as a transitionary LRD would provide smoking-gun evidence for SMBH accretion at the center of at least some fraction, if not all, of this population. Furthermore, the optically thin sight lines down into the central engine of the XRD should exhibit more short-timescale variability than the rest of the LRD population and therefore offer critical constraints on the accretion physics and even black hole masses of the entire LRD population.

Acknowledgments

We would like to thank the anonymous reviewer for their constructive comments, which improved the final manuscript.

We thank Bernd Husemann for his critical contributions to the NIRSpec Wide GTO survey, and in particular his help in selecting high-priority X-ray-luminous targets.

R.E.H. acknowledges support by the German Aerospace Center (DLR) and the Federal Ministry for Economic Affairs and Energy (BMWi) through program 50OR2403 "RUBIES." A.d.G. acknowledges support from a Clay Fellowship awarded by the Smithsonian Astrophysical Observatory. A.J.B. acknowledges funding from the "FirstGalaxies" Advanced grant from the European Research Council (ERC) under the European Union's Horizon 2020 research and innovation program (grant agreement No. 789056). R.P.N. thanks Neil Pappalardo and Jane Pappalardo for their generous support of the MIT Pappalardo Fellowships in Physics. Support for this work was provided by the Brinson Foundation through a Brinson Prize Fellowship grant. H.Ü. acknowledges funding by the European Union (ERC APEX, 101164796). Views and opinions expressed are, however, those of the authors only and do not necessarily reflect those of the European Union or the European Research Council Executive Agency. Neither the European Union nor the granting authority can be held responsible for them. G.V. acknowledges support from European Union's HE ERC Starting grant No. 101040227—WINGS. B.W. acknowledges support provided by NASA through Hubble Fellowship grant HST-HF2-51592.001 awarded by the Space Telescope Science Institute, which is operated by the Association of Universities for Research in Astronomy, In., for NASA, under the contract NAS 5-26555.

The data products presented herein were retrieved from the Dawn JWST Archive (DJA). DJA is an initiative of the Cosmic Dawn Center (DAWN).

This work is based in part on observations made with the NASA/ESA/CSA James Webb Space Telescope. The data were obtained from the Mikulski Archive for Space Telescopes at the Space Telescope Science Institute, which is operated by the Association of Universities for Research in Astronomy, Inc., under NASA contract NAS 5-03127 for JWST. These observations are associated with programs Nos. GTO-1213. The data described here may be obtained from the MAST archive at DOI: 10.17909/qffz-b324.

This Letter employs a list of Chandra datasets, obtained by the Chandra X-ray Observatory, contained in DOI: 10.25574/cdc.540.

This work is based on observations taken by the 3D-HST Treasury Program (GO 12177 and 12328) with the NASA/ESA HST, which is operated by the Association of Universities for Research in Astronomy, Inc., under NASA contract NAS5-26555.

This work makes use of color palettes created by Martin Krzywinski designed for colorblindness. The color palettes and more information can be found at http://mkweb.bcgsc.ca/colorblind/.

Facilities: CXO (ACIS), HST (ACS, WFC3), CFHT (WIRCam), JWST (NIRSpec), Spitzer (IRAC, MIPS), JCMT (SCUBA).

Software: `Astropy` (Astropy Collaboration et al. 2013, 2018, 2022), `dust_attenuation`, `dust_extinction` (K. Gordon 2024), `jax` (J. Bradbury et al. 2018), LaTeX (L. Lamport 1994), `Matplotlib` (J. D. Hunter 2007), `NumPy` (T. E. Oliphant 2006; S. van der Walt et al. 2011; C. R. Harris et al. 2020), `NumPyro` (D. Phan et al. 2019), `scipy` (P. Virtanen et al. 2020), `sedpy` (B. Johnson & J. Leja 2017), `specutils` (Astropy-Specutils Development Team 2019), `unite` (R. E. Hviding 2025).

Appendix A
X-Ray Modeling

We utilize the Chandra ACIS data from the DEEP2 survey (A. D. Goulding et al. 2012). The source was observed between dates 2005 March 24 and 2008 June 23 for a total of 29 individual observations. Photons were extracted following the procedure outlined in A. D. Goulding et al. (2012) of the astrometry-corrected merged Level 2 events file and from a circular aperture with radius consistent with the 90% encircled energy fraction of the combined PSF. The background region was contemplated from an annulus with an inner radius of 1.3× the PSF radius and an outer radius of 5× the PSF radius excluding the presence of any nearby bright sources. Necessary instrument response files were extracted and combined from the individual ObsIDs.

The spectrum was extracted from the stacked multiepoch observations to maximize the S/N. We performed spectral fitting using XSPEC (K. A. Arnaud 1996) minimizing the Cash statistic (W. Cash 1979) with a model consisting of an absorbed power law with both Galactic and intrinsic absorption components: `model = phabs*(zphabs*zpow)`. The Galactic absorption column density was fixed to the known $N_{\mathrm{H,MW}} = 9.25 \times 10^{19}\,\mathrm{cm}^{-2}$. The fit results, summarized in Table 1, indicate a typical AGN spectrum with a photon index of $\Gamma \approx 1.8$ and an intrinsic luminosity of $L_{2-10\,\mathrm{keV}} \approx 1.5 \times 10^{44}\,\mathrm{erg\,s}^{-1}$. The source shows moderate intrinsic absorption with $N_{\mathrm{H}} \approx 2.4 \times 10^{22}\,\mathrm{cm}^{-2}$. Although the individual measurements have significant uncertainties, together they indicate weak evidence for variability, specifically the null hypothesis is rejected at the 90% (1.6σ) level, potentially similar to the X-ray variability seen in S. Fu et al. (2025).

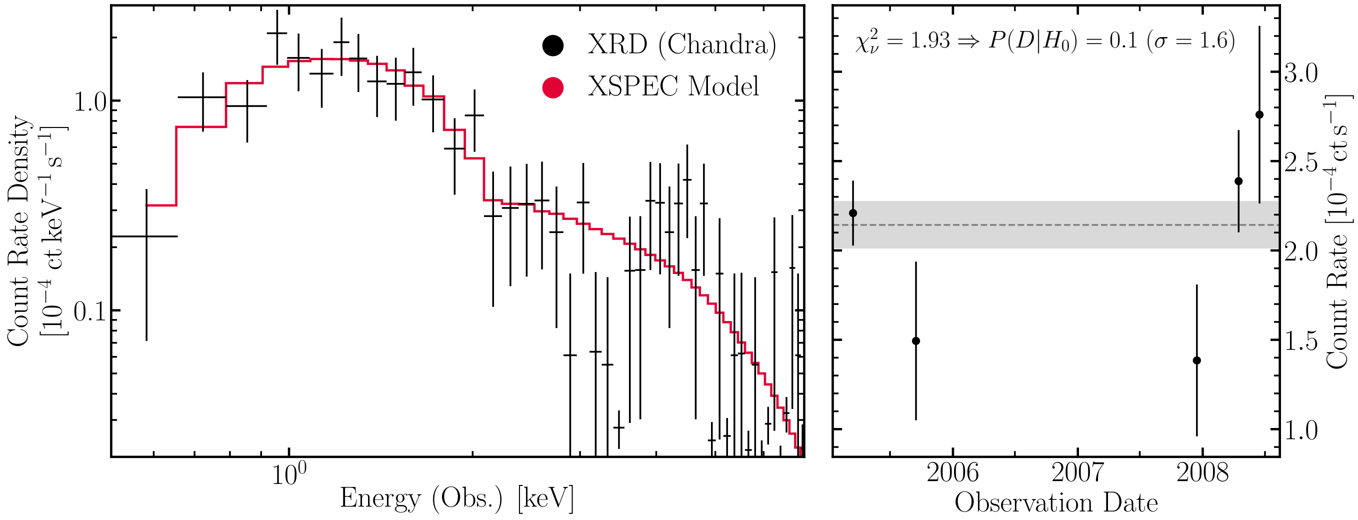

Figure A1. X-ray properties of the XRD. Left: the Chandra ACIS-I X-ray spectrum (black) with the best-fit absorbed power-law model (red). The spectrum is consistent with a typical AGN ($L_{2-10\,\mathrm{keV}} \sim 10^{44}\,\mathrm{erg\,s}^{-1}$ and $\Gamma \sim 1.8$) with moderate absorption ($N_{\mathrm{H}} \sim 10^{22}\,\mathrm{cm}^{-2}$). Right: the long-term X-ray light curve in the observed 0.5−7 keV band. The dashed line and gray region show the weighted mean and error on the weighted mean, respectively. The sources shows weak evidence for variability, specifically the null hypothesis is rejected at the 90% (1.6σ) level.

Appendix B
Emission-line Fitting

We perform a detailed emission-line analysis using the `unite` (R. E. Hviding 2025) spectral fitting code. A key feature of our analysis is the simultaneous fitting of the PRISM, G235H, and G395H spectra. This approach allows us to leverage the high S/N of the PRISM data to constrain the continuum and broad-line wings while using the high-resolution grating data to resolve narrow-line components and kinematic substructure. The fitting procedure explicitly accounts for the wavelength-dependent LSF of each disperser and integrates each pixel to account for the critical undersampling of the NIRSpec LSF. We use the NIRSpec LSF curves of an idealized point source obtained with `msafit` (A. de Graaff et al. 2024).

We model the emission lines using a combination of narrow and broad components. All lines are tied to a common redshift, and each set of narrow and broad lines shares a common FWHM. For the permitted transitions (Hβ, Hα, Paγ, Paβ, etc.), we test three different line profiles to characterize the broad-line region kinematics: a Gaussian profile, a Lorentzian profile, and an exponential profile. As shown in Figure B1 and Table B1, the non-Gaussian profiles provide a significantly better fit, with the Lorentzian profile preferred at the 2.7σ level based on the relative widely applicable information criteria (WAICs; S. Watanabe & M. Opper 2010), suggesting that the lines show significant non-Gaussian wings. However, we note that the significance of this preference depends on the exact fitting prescription used, such as the choice of priors and the relative independence of the broad- and narrow-component kinematics. Follow-up grating spectroscopy at high S/N would be necessary to differentiate between Lorentzian and exponential wings and to constrain the true shape of the broad components in the emission lines.

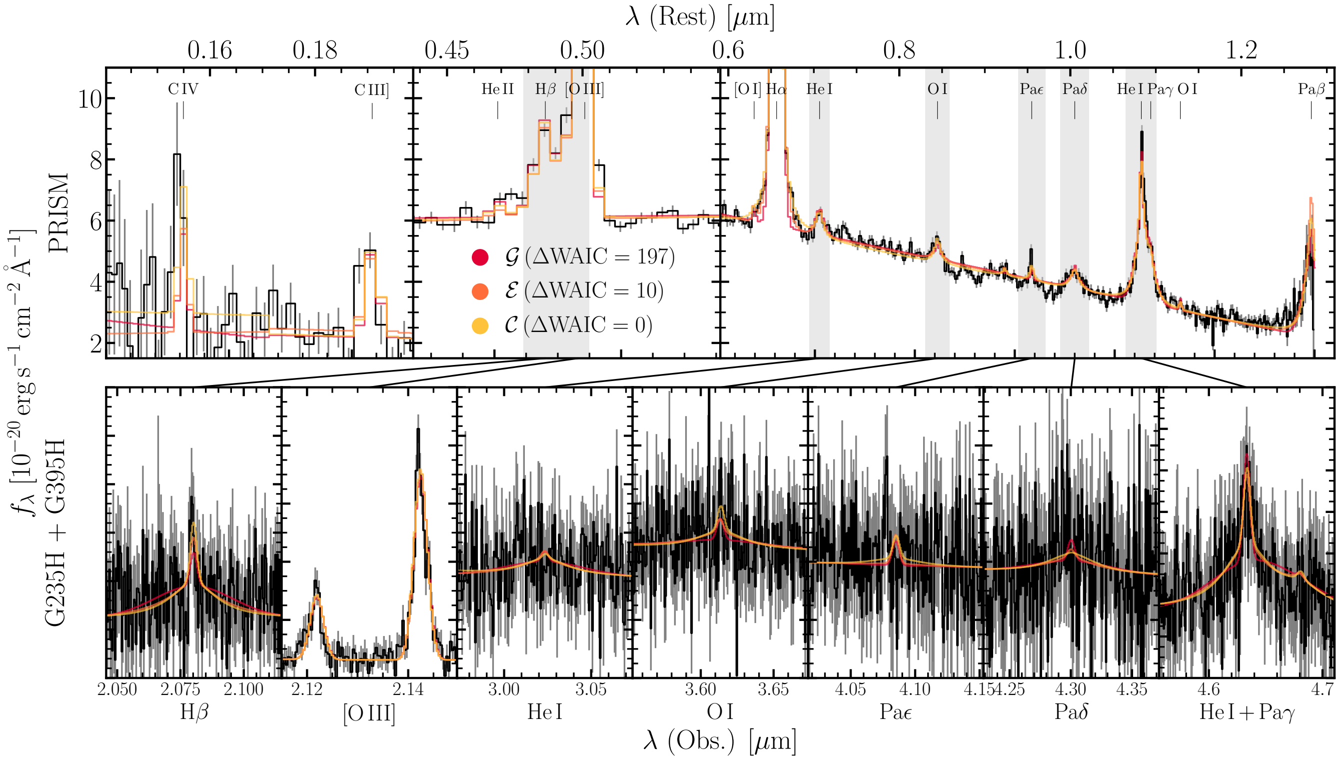

Figure B1. Emission-line fits to the XRD, with `unite` leveraging all three dispersers simultaneously while accounting for wavelength dependence and undersampling of the LSFs. All lines are fit with a narrow component with a common width. Permitted transitions are fit with an additional broad Gaussian (red), Lorentzian (orange), or exponential (yellow) component. The top panels show the PRISM spectrum, whereas the bottom panels show the grating spectra. The Lorentzian and exponential profiles are strongly preferred over the Gaussian model, with Lorentzian wings preferred over exponential wings (~3σ). We note, however, that the statistical significance of this preference depends on the specific fitting assumptions, particularly regarding the kinematic coupling between components.

Table B1
`Unite` Emission-line Fitting Results

	Broad Lorentzian		Broad Exponential		Broad Gaussian	
WAIC	30616		30626		30812	
Redshift	$3.278110^{+0.000095}_{-0.000098}$		$3.278114^{+0.000084}_{-0.000098}$		$3.278121^{+0.000099}_{-0.000097}$	
Narrow FWHM (km s^{-1})	425^{+17}_{-15}		430^{+16}_{-17}		454^{+16}_{-17}	
Broad FWHM (km s^{-1})	3222^{+82}_{-78}		2712^{+57}_{-59}		5070^{+110}_{-100}	
	Narrow-line Fluxes (10^{-20} erg s^{-1} cm^{-2}) and EWs (Å)					
	Flux	EW	Flux	EW	Flux	EW
C IV λ1549	280^{+120}_{-130}	25^{+14}_{-12}	290^{+120}_{-120}	26^{+13}_{-12}	280^{+120}_{-120}	26^{+14}_{-12}
C III λ1909	412^{+68}_{-65}	$43.2^{+8.3}_{-7.7}$	406^{+62}_{-64}	$42.6^{+7.3}_{-7.6}$	410^{+66}_{-64}	$43.1^{+8.4}_{-7.9}$
He II λ4687	92^{+36}_{-35}	$3.6^{+1.4}_{-1.3}$	101^{+39}_{-40}	$3.9^{+1.5}_{-1.5}$	108^{+37}_{-41}	$4.2^{+1.5}_{-1.6}$
Hβ	104^{+56}_{-51}	$4.0^{+2.1}_{-2.0}$	93^{+56}_{-49}	$3.6^{+2.2}_{-1.9}$	152^{+53}_{-54}	$5.9^{+2.0}_{-2.1}$
[O III] λ4960	727^{+16}_{-15}	$28.08^{+0.66}_{-0.64}$	725^{+16}_{-15}	$27.84^{+0.65}_{-0.65}$	736^{+15}_{-16}	$28.27^{+0.65}_{-0.70}$
[O III] λ5008	2165^{+47}_{-45}	$83.6^{+2.0}_{-1.9}$	2160^{+46}_{-46}	$82.9^{+1.9}_{-2.0}$	2194^{+45}_{-47}	$84.2^{+1.9}_{-2.1}$
[O I] λ6302	33^{+30}_{-21}	$1.34^{+1.24}_{-0.84}$	87^{+34}_{-32}	$3.4^{+1.3}_{-1.3}$	95^{+41}_{-38}	$3.7^{+1.6}_{-1.5}$
Hα	387^{+98}_{-103}	$16.0^{+4.0}_{-4.3}$	215^{+96}_{-94}	$8.7^{+3.9}_{-3.8}$	992^{+95}_{-94}	$39.7^{+3.9}_{-3.8}$
He I λ7067	16^{+20}_{-12}	$0.70^{+0.88}_{-0.51}$	15^{+20}_{-11}	$0.62^{+0.86}_{-0.47}$	20^{+26}_{-15}	$0.86^{+1.08}_{-0.62}$
O I λ8446	34^{+24}_{-22}	$1.8^{+1.2}_{-1.1}$	38^{+26}_{-21}	$1.9^{+1.3}_{-1.1}$	54^{+25}_{-22}	$2.7^{+1.2}_{-1.1}$
Paζ	23^{+31}_{-17}	$1.29^{+1.76}_{-0.93}$	25^{+32}_{-19}	$1.4^{+1.7}_{-1.1}$	27^{+28}_{-20}	$1.5^{+1.5}_{-1.1}$
Paϵ	48^{+29}_{-26}	$2.8^{+1.7}_{-1.5}$	52^{+33}_{-28}	$3.0^{+1.9}_{-1.6}$	64^{+28}_{-27}	$3.7^{+1.6}_{-1.5}$
Paδ	19^{+21}_{-13}	$1.20^{+1.30}_{-0.82}$	16^{+20}_{-11}	$1.01^{+1.27}_{-0.69}$	27^{+24}_{-18}	$1.7^{+1.5}_{-1.1}$
He I λ10830	281^{+43}_{-37}	$20.1^{+3.1}_{-2.6}$	249^{+39}_{-40}	$17.5^{+2.8}_{-2.8}$	396^{+40}_{-42}	$27.8^{+2.8}_{-2.9}$
Paγ	37^{+34}_{-26}	$2.7^{+2.5}_{-1.9}$	25^{+28}_{-18}	$1.8^{+2.0}_{-1.3}$	29^{+27}_{-20}	$2.1^{+1.9}_{-1.5}$
O I λ11287	43^{+26}_{-25}	$3.3^{+2.0}_{-1.9}$	52^{+24}_{-25}	$4.0^{+1.9}_{-1.9}$	53^{+26}_{-25}	$4.1^{+2.0}_{-1.9}$
Paβ	70^{+96}_{-52}	$7.5^{+10.3}_{-5.5}$	71^{+100}_{-53}	$7.6^{+10.7}_{-5.6}$	123^{+147}_{-90}	$13.2^{+15.8}_{-9.7}$
	Broad-line Fluxes (10^{-20} erg s^{-1} cm^{-2}) and EWs (Å)					
Hβ	1490^{+110}_{-140}	$57.6^{+4.5}_{-5.3}$	1290^{+110}_{-100}	$49.7^{+4.2}_{-4.2}$	1170^{+110}_{-100}	$44.8^{+4.4}_{-3.9}$
Hα	14930^{+200}_{-210}	$618.7^{+9.6}_{-9.9}$	13210^{+150}_{-190}	$534.5^{+7.7}_{-8.4}$	11530^{+160}_{-170}	$461.5^{+7.3}_{-6.7}$
He I λ7067	465^{+80}_{-87}	$20.3^{+3.6}_{-3.8}$	448^{+75}_{-73}	$19.1^{+3.2}_{-3.1}$	386^{+70}_{-70}	$16.3^{+3.0}_{-3.0}$
O I λ8446	426^{+78}_{-82}	$21.7^{+4.0}_{-4.2}$	292^{+75}_{-72}	$14.5^{+3.8}_{-3.6}$	239^{+74}_{-68}	$11.8^{+3.7}_{-3.3}$
Paζ	80^{+86}_{-85}	$4.5^{+4.8}_{-4.8}$	13^{+75}_{-85}	$0.7^{+4.2}_{-4.7}$	-22^{+74}_{-68}	$-1.2^{+4.0}_{-3.7}$
Paϵ	163^{+88}_{-96}	$9.6^{+5.2}_{-5.6}$	87^{+81}_{-81}	$5.0^{+4.7}_{-4.7}$	43^{+73}_{-78}	$2.5^{+4.2}_{-4.5}$
Paδ	486^{+82}_{-77}	$30.7^{+5.2}_{-4.9}$	406^{+69}_{-72}	$25.2^{+4.3}_{-4.5}$	378^{+64}_{-71}	$23.3^{+3.9}_{-4.4}$
He I λ10830	2500^{+140}_{-140}	179^{+10}_{-10}	2230^{+120}_{-110}	$157.1^{+8.6}_{-8.0}$	1900^{+110}_{-120}	$133.2^{+7.4}_{-8.5}$
Paγ	810^{+110}_{-130}	$58.8^{+8.5}_{-9.7}$	689^{+98}_{-109}	$49.5^{+6.9}_{-7.9}$	714^{+96}_{-98}	$51.0^{+6.9}_{-7.1}$
Paβ	3670^{+500}_{-480}	396^{+57}_{-53}	3120^{+390}_{-450}	336^{+46}_{-48}	2750^{+380}_{-370}	295^{+45}_{-40}

Appendix C
SED Fitting

This appendix provides additional details of the SED fitting discussed in Section 3.2, including the configuration choices for both CIGALE and AGNFitter. As emphasized in Section 3.2, these fits are intentionally performed on the broadband photometry and X-ray constraints.

C.1. CIGALE Configuration

We run CIGALE in `pdf_analysis` mode with the configuration summarized in Table C1. In brief, we adopt a delayed-τ star formation history (`sfhdelayed`), G. Bruzual & S. Charlot (2003) stellar population synthesis (`bc03` with a G. Chabrier 2003 initial mass function), a modified starburst attenuation curve (`dustatt_modified_starburst`), THEMIS dust emission (`themis`; A. P. Jones et al. 2017), and SKIRTOR torus models (`skirtor2016`; M. Stalevski et al. 2012, 2016). We incorporate X-ray constraints using the I. E. López et al. (2024) module (`lopez24`), which ties $L_{2-10\,\mathrm{keV}}$ to the mid-IR luminosity through an α_{irx} parameter and generates an intrinsic AGN X-ray spectrum. Upper limits are included using CIGALE's upper-limit treatment (we use the `full` option). Reported parameter values in Table C1 correspond to the CIGALE Bayesian estimates.

C.2. AGNFitter Configuration

We fit the same photometric data with AGNFitter (G. Calistro Rivera et al. 2016) using the radio-to-X-ray extension described in L. N. Martínez-Ramírez et al. (2024). The model decomposes the SED into four components: a stellar population, cold dust associated with star formation, an accretion disk ("big blue bump"), and a dusty torus. For the component templates we use G. Bruzual & S. Charlot (2003) stellar populations, C. Schreiber et al. (2017) star-forming dust templates, the accretion disk models of M. J. Temple et al. (2021), and SKIRTOR torus models. As narrow and broad emission lines are included with the M. J. Temple et al. (2021) model, the accretion disk extinction is also applied to the emission lines. The implied AGN X-ray luminosity is linked to the mid-IR (6 μm) luminosity using the D. Stern (2015) relation, enabling a direct

Table C1
CIGALE Configuration and Results

Parameter Name	Unit	Grid/Option	Measured Value
Star Formation History: Delayed Star Formation			
Main *e*-fold time ($\tau_{\rm main}$)	Myr	3000, 5000, 7000, 9000, 11000	6000 ± 2800
Main age (age$_{\rm main}$)	Myr	100, 500, 1000, 3000	1000.0 ± 0.25
Burst fraction ($f_{\rm burst}$)	⋯	0.0	⋯
Normalize	⋯	True	⋯
Stellar mass ($M_\star$)	$M_\odot$	⋯	$(2.48 \pm 0.12) \times 10^{10}$
Simple Stellar Population: G. Bruzual & S. Charlot (2003)			
Initial mass function	⋯	1 (G. Chabrier 2003)	⋯
Metallicity	Z	0.008, 0.02	0.00800 ± 0.00021
Separation age	Myr	10	⋯
Dust Attenuation: Modified D. Calzetti et al. (2000)			
$E(B-V)_{\rm lines}$	mag	0.1, 0.3, 0.5, 0.7, 0.9	0.7
Extinction factor ($f_{E(B-V)}$)	⋯	0.1, 0.44, 0.7	0.7
UV bump wavelength	nm	217.5	⋯
UV bump width	nm	35.0	⋯
UV bump amplitude	⋯	0.0	⋯
Power-law slope	⋯	−0.4, 0.0	−0.4
Dust Emission: THEMIS (A. P. Jones et al. 2017)			
Hydrocarbon mass fraction ($q_{\rm hac}$)	⋯	0.02, 0.17, 0.24	0.02000 ± 0.00014
Minimum radiation field ($U_{\rm min}$)	⋯	0.1, 1.0, 10.0, 50.0	30 ± 20
Power-law slope (α)	⋯	2.1, 2.5, 2.9	2.67 ± 0.24
Illumination fraction (γ)	⋯	0.4	⋯
AGN Structure: SKIRTOR (M. Stalevski et al. 2012, 2016)			
Optical depth ($\tau_{9.7\mu{\rm m}}$)	⋯	3, 7, 11	8.0 ± 3.0
Radial gradient (p)	⋯	1.0	⋯
Polar gradient (q)	⋯	1.0	⋯
Opening angle ($\theta_{\rm open}$)	deg	20, 40, 60, 80	70 ± 14
Radius ratio ($R_{\rm out}/R_{\rm in}$)	⋯	10, 20, 30	18.0 ± 7.5
Clump mass fraction ($M_{\rm cl}$)	⋯	0.97	⋯
Inclination (i)	deg	10, 30, 50, 70, 90	73 ± 20
Disk type	⋯	2 (I. E. López et al. 2024)	⋯
Disk tuning parameter (δ)	⋯	0, 0.25, 0.5	0.24 ± 0.21
AGN fraction	⋯	0.1, 0.3, 0.5, 0.7, 0.9	0.1002 ± 0.0061
Polar $E(B-V)$	mag	0.00	⋯
X-Ray: I. E. López et al. (2024)			
Photon index (Γ)	⋯	1.8	⋯
Cutoff energy ($E_{\rm cut}$)	keV	300	⋯
$\alpha_{\rm irx}$ deviation	dex	0, 0.15, 0.3, 0.45, 0.6	0.017 ± 0.050
Low-mass X-ray binary deviation	dex	0.0	⋯
High-mass X-ray binary deviation	dex	0.0	⋯

Table C2
AGNFitter Configuration and Results

Parameter Name	Unit	Measured Value
Galaxy: G. Bruzual & S. Charlot (2003)		
Metallicity	Z	$0.77^{+0.68}_{-0.48}$
e-fold time (τ)	⋯	$4.0^{+3.3}_{-2.5}$
Age	Myr	720^{+760}_{-610}
$E(B-V)_{\rm gal}$	mag	$0.153^{+0.097}_{-0.070}$
Stellar mass ($M_\star$)	$M_\odot$	$(1.4^{+2.6}_{-1.2}) \times 10^9$
Starburst: C. Schreiber et al. (2017)		
Dust temperature	K	$31.2^{+7.4}_{-10.1}$
PAH fraction ($f_{\rm PAH}$)	⋯	$0.027^{+0.018}_{-0.018}$
Big Blue Bump: M. J. Temple et al. (2021)		
$E(B-V)_{\rm BBB}$	mag	$0.885^{+0.018}_{-0.020}$
Torus: SKIRTOR (M. Stalevski et al. 2012, 2016)		
Optical depth ($\tau_{\rm v}$)	⋯	$10.47^{+0.35}_{-0.34}$
Opening angle (oa)	deg	$12.66^{+1.69}_{-1.79}$
Inclination (i)	deg	$30.14^{+3.53}_{-3.50}$

comparison between the XRD's observed L_2–10 keV and the model-predicted value. Posterior summaries for key parameters are given in Table C2.

ORCID iDs

Raphael E. Hviding https://orcid.org/0000-0002-4684-9005
Anna de Graaff https://orcid.org/0000-0002-2380-9801
Hanpu Liu (刘翰溥) https://orcid.org/0000-0003-2488-4667
Andy D. Goulding https://orcid.org/0000-0003-4700-663X
Yilun Ma (马逸伦) https://orcid.org/0000-0002-0463-9528
Jenny E. Greene https://orcid.org/0000-0002-5612-3427
Leindert A. Boogaard https://orcid.org/0000-0002-3952-8588
Andrew J. Bunker https://orcid.org/0000-0002-8651-9879
Nikko J. Cleri https://orcid.org/0000-0001-7151-009X
Marijn Franx https://orcid.org/0000-0002-8871-3026
Michaela Hirschmann https://orcid.org/0000-0002-3301-3321
Joel Leja https://orcid.org/0000-0001-6755-1315
Jorryt Matthee https://orcid.org/0000-0003-2871-127X
Rohan P. Naidu https://orcid.org/0000-0003-3997-5705
David J. Setton https://orcid.org/0000-0003-4075-7393
Hannah Übler https://orcid.org/0000-0003-4891-0794
Giacomo Venturi https://orcid.org/0000-0001-8349-3055
Bingjie Wang (王冰洁) https://orcid.org/0000-0001-9269-5046

References

Akins, H. B., Casey, C. M., Berg, D. A., et al. 2025, ApJL, 980, 29
Akins, H. B., Casey, C. M., Lambrides, E., et al. 2025, ApJ, 991, 37
Ananna, T. T., Bogdán, A., Kovács, O. E., Natarajan, P., & Hickox, R. C. 2024, ApJ, 969, L18
Arnaud, K. A. 1996, ASPC, 101, 17

Astropy Collaboration, Price-Whelan, A. M., Lim, P. L., et al. 2022, ApJ, 935, 167

Astropy Collaboration, Price-Whelan, A. M., Sipőcz, B. M., et al. 2018, AJ, 156, 123

Astropy Collaboration, Robitaille, T. P., Tollerud, E. J., et al. 2013, A&A, 558, A33

Astropy-Specutils Development Team 2019, Specutils: Spectroscopic analysis and reduction, Astrophysics Source Code Library, ascl:1902.012

Begelman, M. C., & Dexter, J. 2026, ApJ, 996, 48

Boquien, M., Burgarella, D., Roehlly, Y., et al. 2019, A&A, 622, A103

Bradbury, J., Frostig, R., Hawkins, P., et al. 2018, JAX: Composable transformations of Python+NumPy programs, GitHub, https://github.com/jax-ml/jax

Brammer, G. 2023, Msaexp: NIRSpec analysis tools, v0.6.17, Zenodo, doi:10.5281/zenodo.8319596

Brammer, G., & Valentino, F. 2025, The DAWN JWST Archive: Compilation of Public NIRSpec Spectra, Zenodo, doi:10.5281/zenodo.15472354

Brammer, G. B., van Dokkum, P. G., Franx, M., et al. 2012, ApJS, 200, 13

Brandt, W. N., & Alexander, D. M. 2015, A&ARv, 23, 1

Bruzual, G., & Charlot, S. 2003, MNRAS, 344, 1000

Burgarella, D., Buat, V., & Iglesias-Páramo, J. 2005, MNRAS, 360, 1413

Calistro Rivera, G., Lusso, E., Hennawi, J. F., & Hogg, D. W. 2016, ApJ, 833, 98

Calzetti, D., Armus, L., Bohlin, R. C., et al. 2000, ApJ, 533, 682

Casey, C. M., Akins, H. B., Kokorev, V., et al. 2024, ApJ, 975, L4

Cash, W. 1979, ApJ, 228, 939

Chabrier, G. 2003, PASP, 115, 763

Chang, S.-J., Gronke, M., Matthee, J., & Mason, C. 2026, MNRAS, 545, staf2131

Chevallard, J., Charlot, S., Wandelt, B., & Wild, V. 2013, MNRAS, 432, 2061

Chira, M., Georgakakis, A., Ruiz, A., et al. 2026, MNRAS, 545, staf1905

Czerny, B., Li, J., Loska, Z., & Szczerba, R. 2004, MNRAS, 348, L54

Davis, M., Guhathakurta, P., Konidaris, N. P., et al. 2007, ApJ, 660, L1

de Graaff, A., Brammer, G., Weibel, A., et al. 2025a, A&A, 697, A189

de Graaff, A., Hviding, R. E., Naidu, R. P., et al. 2025b, arXiv:2511.21820

de Graaff, A., Rix, H.-W., Carniani, S., et al. 2024, A&A, 684, A87

de Graaff, A., Rix, H.-W., Naidu, R. P., et al. 2025c, A&A, 701, A168

D'Eugenio, F., Maiolino, R., Perna, M., et al. 2025, arXiv:2503.11752

Dong, X., Wang, T., Wang, J., et al. 2008, MNRAS, 383, 581

Duras, F., Bongiorno, A., Ricci, F., et al. 2020, A&A, 636, A73

Fu, S., Zhang, Z., Jiang, D., et al. 2025, arXiv:2512.02096

Gandhi, P., Horst, H., Smette, A., et al. 2009, A&A, 502, 457

Gaskell, C. M., Goosmann, R. W., Antonucci, R. R. J., & Whysong, D. H. 2004, ApJ, 616, 147

Geach, J. E., Dunlop, J. S., Halpern, M., et al. 2017, MNRAS, 465, 1789

Glikman, E., Helfand, D. J., & White, R. L. 2006, ApJ, 640, 579

Gordon, K. 2024, JOSS, 9, 7023

Gordon, K. D., Clayton, G. C., Misselt, K. A., Landolt, A. U., & Wolff, M. J. 2003, ApJ, 594, 279

Goulding, A. D., Forman, W. R., Hickox, R. C., et al. 2012, ApJS, 202, 6

Greene, J. E., & Ho, L. C. 2005, ApJ, 630, 122

Greene, J. E., Setton, D. J., Furtak, L. J., et al. 2026, ApJ, 996, 129

Gunasekera, C. M., van Hoof, P. A. M., Dehghanian, M., et al. 2025, RMxAA, 61, 120

Hao, H., Elvis, M., Civano, F., et al. 2010, ApJ, 724, L59

Harris, C. R., Millman, K. J., van der Walt, S. J., et al. 2020, Natur, 585, 357

Heintz, K. E., Brammer, G. B., Watson, D., et al. 2025, A&A, 693, A60

Hickox, R. C., & Alexander, D. M. 2018, ARA&A, 56, 625

Hirschmann, M., Charlot, S., Feltre, A., et al. 2019, MNRAS, 487, 333

Horne, K. 1986, PASP, 98, 609

Hunter, J. D. 2007, CSE, 9, 90

Hviding, R. E. 2025, TheSkyentist/unite: v0, Zenodo, doi:10.5281/zenodo.15585035

Hviding, R. E., de Graaff, A., Miller, T. B., et al. 2025, A&A, 702, A57

Inayoshi, K. 2025, ApJ, 988, L22

Inayoshi, K., & Maiolino, R. 2025, ApJ, 980, L27

Ji, X., Maiolino, R., Übler, H., et al. 2025, MNRAS, 544, 3900

Jin, C., Ward, M., & Done, C. 2012, MNRAS, 422, 3268

Johnson, B., & Leja, J. 2017, Bd-j/prospector: Initial release, v0.1, Zenodo, doi:10.5281/zenodo.1116491

Jones, A. P., Köhler, M., Ysard, N., Bocchio, M., & Verstraete, L. 2017, A&A, 602, A46

Juodžbalis, I., Ji, X., Maiolino, R., et al. 2024, MNRAS, 535, 853

Kido, D., Ioka, K., Hotokezaka, K., Inayoshi, K., & Irwin, C. M. 2025, MNRAS, 544, 3407

Kocevski, D. D., Finkelstein, S. L., Barro, G., et al. 2025, ApJL, 986, 126

Kokorev, V., Caputi, K. I., Greene, J. E., et al. 2024, ApJ, 968, 38

Korista, K. T., & Goad, M. R. 2004, ApJ, 606, 749

Krawczyk, C. M., Richards, G. T., Gallagher, S. C., et al. 2015, AJ, 149, 203

Labbe, I., Greene, J. E., Matthee, J., et al. 2024, arXiv:2412.04557

Lambrides, E., Garofali, K., Larson, R., et al. 2024, arXiv:2409.13047

Lamport, L. 1994, LaTeX: A Document Preparation System (2nd ed.; Addison-Wesley Professional)

Leighly, K. M., Gallagher, S. C., Choi, H., et al. 2025, ApJ, 993, 129

Leighly, K. M., Terndrup, D. M., Baron, E., et al. 2014, ApJ, 788, 123

Li, Z.-J., Zou, S., Lyu, J., et al. 2025, arXiv:2512.02093

Liu, H., Jiang, Y.-F., Quataert, E., Greene, J. E., & Ma, Y. 2025, ApJ, 994, 113

Liu, H., Jiang, Y.-F., Quataert, E., et al. 2026, arXiv:2603.02317

López, I. E., Yang, G., Mountrichas, G., et al. 2024, A&A, 692, A209

Ma, Y., Greene, J. E., Setton, D. J., et al. 2025a, ApJ, 981, 191

Ma, Y., Greene, J. E., Setton, D. J., et al. 2025b, arXiv:2504.08032

Madau, P., & Haardt, F. 2024, ApJ, 976, L24

Maiolino, R., Marconi, A., Salvati, M., et al. 2001, A&A, 365, 28

Maiolino, R., Risaliti, G., Signorini, M., et al. 2025, MNRAS, 538, 1921

Martínez-Ramírez, L. N., Calistro Rivera, G., Lusso, E., et al. 2024, A&A, 688, A46

Maseda, M. V., de Graaff, A., Franx, M., et al. 2024, A&A, 689, A73

Matthee, J., Naidu, R. P., Brammer, G., et al. 2024, ApJ, 963, 129

Naidu, R. P., Matthee, J., Katz, H., et al. 2025, arXiv:2503.16596

Noll, S., Burgarella, D., Giovannoli, E., et al. 2009, A&A, 507, 1793

Oliphant, T. E. 2006, A guide to NumPy, Vol. 1 (Trelgol Publishing)

Phan, D., Pradhan, N., & Jankowiak, M. 2019, arXiv:1912.11554

Rinaldi, P., Bonaventura, N., Rieke, G. H., et al. 2025, ApJ, 992, 71

Rusakov, V., Watson, D., Nikopoulos, G. P., et al. 2026, Natur, 649, 574

Salim, S., Boquien, M., & Lee, J. C. 2018, ApJ, 859, 11

Santarelli, A. D., Farag, E., Bellinger, E. P., et al. 2026, ApJL, 998, L4

Schreiber, C., Elbaz, D., Pannella, M., et al. 2017, A&A, 602, A96

Setton, D. J., Greene, J. E., de Graaff, A., et al. 2025, ApJ, 995, 118

Setton, D. J., Greene, J. E., Spilker, J. S., et al. 2025, ApJL, 991, L10

Skelton, R. E., Whitaker, K. E., Momcheva, I. G., et al. 2014, ApJS, 214, 24

Stalevski, M., Fritz, J., Baes, M., Nakos, T., & Popović, L. 2012, MNRAS, 420, 2756

Stalevski, M., Ricci, C., Ueda, Y., et al. 2016, MNRAS, 458, 2288

Stern, D. 2015, ApJ, 807, 129

Taylor, A. J., Kokorev, V., Kocevski, D. D., et al. 2025, ApJL, 989, L7

Temple, M. J., Hewett, P. C., & Banerji, M. 2021, MNRAS, 508, 737

Torralba, A., Matthee, J., Pezzulli, G., et al. 2026, A&A, 707, A75

Tortosa, A., Ricci, C., Ho, L. C., et al. 2023, MNRAS, 519, 6267

Umeda, H., Inayoshi, K., Harikane, Y., & Murase, K. 2026, ApJ, 999, 183

van der Walt, S., Colbert, S. C., & Varoquaux, G. 2011, CSE, 13, 22

Van Der Wel, A., Bell, E. F., Häussler, B., et al. 2012, ApJS, 203, 12

Vanden Berk, D. E., Richards, G. T., Bauer, A., et al. 2001, AJ, 122, 549

Virtanen, P., Gommers, R., Oliphant, T. E., et al. 2020, NatMe, 17, 261

Wang, B., de Graaff, A., Davies, R. L., et al. 2025, ApJ, 984, 121

Wang, B., Leja, J., de Graaff, A., et al. 2024, ApJ, 969, L13

Watanabe, S., & Opper, M. 2010, JMLR, 11, 3571

Williams, C. C., Alberts, S., Ji, Z., et al. 2024, ApJ, 968, 34

Yan, Z., Inayoshi, K., Chen, K., & Guo, J. 2025, arXiv:2512.11050

Yang, G., Boquien, M., Buat, V., et al. 2020, MNRAS, 491, 740

Yue, M., Eilers, A.-C., Ananna, T. T., et al. 2024, ApJ, 974, L26